PNAS
www.pnas.org

Supplementary Information for

Rapid ocean acidification and pH rebound following the end-Cretaceous Chicxulub impact

Michael J. Henehan*, Andy Ridgwell, Ellen Thomas, Shuang Zhang, Laia Alegret, Daniela N. Schmidt, James W. B. Rae, James D. Witts, Neil H. Landman, Sarah E. Greene, Brian T. Huber, James Super, Noah J. Planavsky and Pincelli M. Hull*

***Corresponding Authors: Michael Henehan and Pincelli Hull.**
Email: henehan@gfz-potsdam.de or pincelli.hull@yale.edu

This PDF file includes:

Supplementary text
Figs. S1 to S24
Tables S1 to S3
References for SI reference citations

www.pnas.org/cgi/doi/10.1073/pnas.1905989116

Supporting Information Text

1. Sampling

A. Sample Sites. The K-Pg boundary presents a challenge for palaeoceanographic reconstruction, as there is near-complete elimination of Cretaceous planktic foraminiferal species at the boundary, with post-extinction fauna dwarfed and thin walled. The few taxa that do cross the boundary are generally too rare and small to obtain the material necessary for boron isotope analysis (1-3 mg, see Fig SS11). In addition, there is a dramatic shift in the quality of carbonate preservation globally across the K-Pg: uppermost Cretaceous foraminifera are often poorly-preserved (22), while earliest Paleocene deep-sea sediments often contain plentiful well-preserved but minute foraminifera. In addition, deep-sea sedimentation rates in the early Paleocene are greatly reduced (e.g. ref. (40)), making it difficult to capture the geologically-instantaneous processes posited to have occurred directly after impact (e.g. (20, 21)). To obtain a record across the event, therefore, we needed to combine samples from a range of mid-low latitude sites, from shallow shelf sites facing the open ocean to open Pacific (Fig. S1).

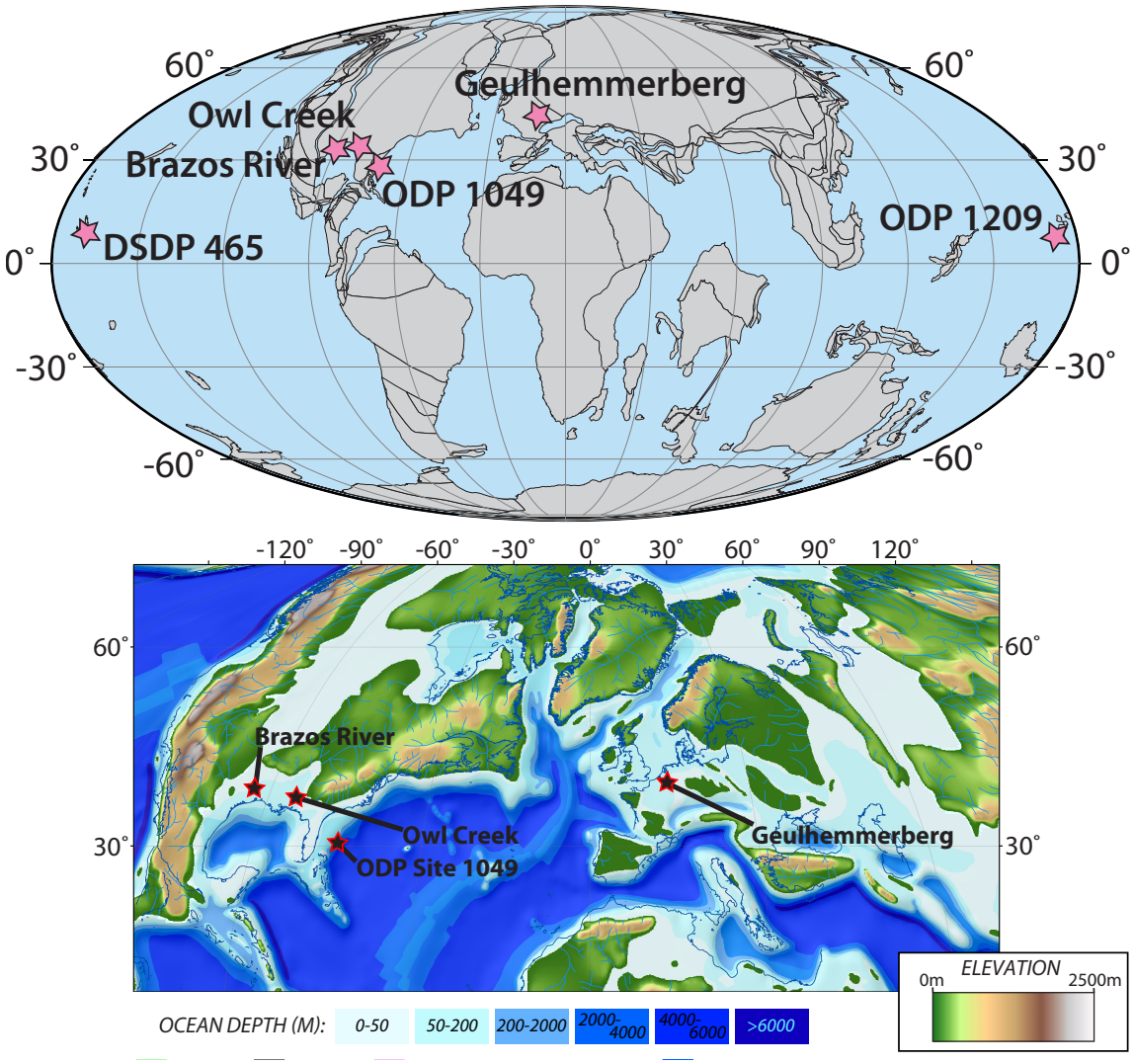

Fig. S1. Locations of our sample sites. A global K-Pg boundary projection from ODSN Paleomap, above, shows the locations of our sample sites as pink stars. Note the grey areas are the positions of plate fragments (with plate fragment boundaries marked as thin black lines) and do not translate to sub-aerial exposure. To better show the marine setting of the sample sites, below the global projection, we plot our Atlantic-region sites on the Maastrichtian palaeogeographic reconstruction from (41) which forms the basis of our cGENIE configuration.

Of these sites, one shallow marine sample location (Geulhemmerberg, Netherlands) may preserve the first 10^2-10^3yr after bolide impact (6), allowing us to investigate transient impact-induced K-Pg surface ocean acidification otherwise unresolvable in deep marine records. Other data comes from mixed-layer foraminifera from shelf (Owl Creek (7, 42) and Brazos River (8)) and deep-sea sites (DSDP Site 465, ODP Sites 1209 and 1049). ODP Site 1209 is one of few deep marine K-Pg boundary sites that preserve the abundant, well-preserved epifaunal benthic and shallow planktic foraminifera required for boron isotope analysis, allowing us to test for changes in vertical pH gradient. More details of sample sites are listed in Table S1 below.

Sample site	Latitude (°N)	Longitude (°E)	Palaeo-Latitude (°N)	Palaeo-Longitude (°E)	Present-Day Water Depth (m)	Palaeo-Water Depth (m)	References & notes
ODP Site 1209, Shatsky Rise	32.652	158.506	∼10	∼175	2387	∼2500	(43–45)
DSDP 465, Hess Rise	33.821	178.919	∼16	∼ -175	2161	∼1500	(46–49)
Geulhemmerberg Cave	50.865	5.784	∼ 45	∼ -10	Terrestrial	Above wave base	'E'-clay from ref. (6)
ODP 1049, Blake Nose	30.142	-76.112	∼ 30	∼ -70	2671	1500-1600	(50)
Owl Creek, Mississippi	34.056	-88.924	∼ 33	∼81	Terrestrial	70-150	Sampled 2m from creek level, (7, 42)
Brazos River, Texas	31.108	-96.837	∼ 32	∼90	Terrestrial	30-100	Darting Minnow Creek, (8, 51)

Table S1. Location and details of sample locations used in this study. See also Fig S1.

While it would be preferable to sample continuously at one site across the K-Pg, limitations at each site make this impossible:

- At **ODP Site 1209**, preservation of Cretaceous foraminifera is prohibitively poor. Elsewhere low rates of Cretaceous foraminiferal fragmentation were reported (22), but re-examination revealed that these undamaged foraminifera were Danian and originated from down-core drilling contamination. In fact, Cretaceous planktic foraminifera are almost completely dissolved and not present in abundances required for boron isotope analysis. Some benthic foraminifera are preserved, but it is impossible to ascertain to what extent they are also the product by down-core transport, and hence we refrain from generating a Cretaceous record from this site. Lowermost Danian preservation, however, is excellent, with almost no fragmentation (22, 52) and high Sr/Ca ratios > 1.3 mmol/mol suggesting little or no recrystallisation (53). Epifaunal benthic foraminifera are also abundant.

- At **DSDP Site 465**, fragmentation is similarly high in the Cretaceous, and sample material is recrystallised (with Sr/Ca ratios < 1). There is no sign of significant down-core contamination, but disturbance due to rotary drilling around the K-Pg boundary (46) makes high-resolution stratigraphy around the boundary impossible.

- At **ODP Site 1049**, preservation of foraminifera is very good, but epifaunal benthic foraminifera are too few for boron isotope analysis, rendering this site inappropriate for testing vertical pH gradients. In addition, Biozone P0 is absent, there is extensive reworking, and slumping and sediment deformation are evident in the uppermost Maastrichtian (54, 55).

- At **Geulhemmerberg Cave**, a remarkable snapshot is preserved of the aftermath of the K-Pg event, within thick seams of boundary clay (6). Preservation of foraminifera in this clay bed is 'glassy' (56), typical of foraminifera encased in clay-rich sediments, as seen on the East African margin (57) and Demerara Rise (58). However, the clay bed overlies a disconformity, and under- and overlying sediments primarily comprise carbonate hardground and bioclastic grainstone deposits, containing very scarce, badly preserved foraminiferal remains (59). While a shallow site, the nannofossil assemblage includes typical taxa found elsewhere in the Tethys and Atlantic, indicating communication with the open ocean (60). There is debate on the exact age of the clay layers at this site, but we consider the evidence for deposition directly after impact acceptable (see Section B). A special issue of *Geologie en Mijnbouw* devoted entirely to this section, and containing details of its depositional setting, stratigraphy and sedimentology, is accessible via the *Koninklijk Nederlands Geologisch Mijnbouwkundig Genootschap* archives (Vol. 75, Nos. 2-3, 1996).

- **Owl Creek** is a site on the open margin of the Gulf of Mexico. Molluscan assemblages are very diverse and similar to those seen along the entire margin, from Texas to the New Jersey margin (42, 61, 62), indicating unrestricted communication with the open-ocean. Preservation of foraminifera at this site is excellent, with glassy foraminifera preserved alongside ammonites with intact primary nacre (42). However, no K-Pg boundary clay is preserved at this site. The boundary is marked by an erosional unconformity at the contact between the Owl Creek and Clayton Formations. The uppermost Maastrichtian is likely absent, and above the boundary only ∼1m of the Clayton formation is present, in which modern vegetation is growing.

- At **Brazos River**, preservation of foraminifera is variable, but in samples with enough foraminifera present to analyse, preservation is excellent. However, sedimentation across the K-Pg boundary is complex and unlikely to be continuous. Sediments of the Corsicana Formation recording mid-shelf deposition are overlain by an erosional surface (13, 63, 64), followed by tens of cm of siliciclastic storm deposits (see Fig. S2), interpreted to represent a mixture of earthquake-generated debris flows and storm or tsunami deposition related to the Chicxulub impact event (13, 63, 65). Both the impact ejecta bed and the overlying 'Hummocky Cross-stratified Sandstone' (8) layers are barren of planktic foraminifera, with only rare fragments of calcareous benthic foraminifera to be found in the > 125 μm size fraction (although we note that Hart et al. (13) report the presence of well-preserved benthic foraminifera in intercalated mudstone layers, which we did not sample).

- At **ODP Site 1267**, where there is a more-or-less continuous K-Pg boundary, we analysed some material but found it to be pervasively diagenetically altered. Trends within and between species appeared to be similar to those seen at Blake Nose, but absolute values of δ^{11}B are anomalously low. Mn/Ca ratios are very high ($>$1000 μmol/mol), and Sr/Ca very low, indicating pervasive recrystallisation and geochemical alteration (53, 66). Indeed, foraminiferal carbonate from this site remained faintly rusty red in colour, even after repeated

alternation of oxidative (Hydrogen peroxide) and reductive (Hydroxylamine hydrochloride) cleaning steps. Therefore, we view the anomalously light absolute δ^{11}B values at this site as the result of pervasive diagenetic alteration, and do not interpret them here.

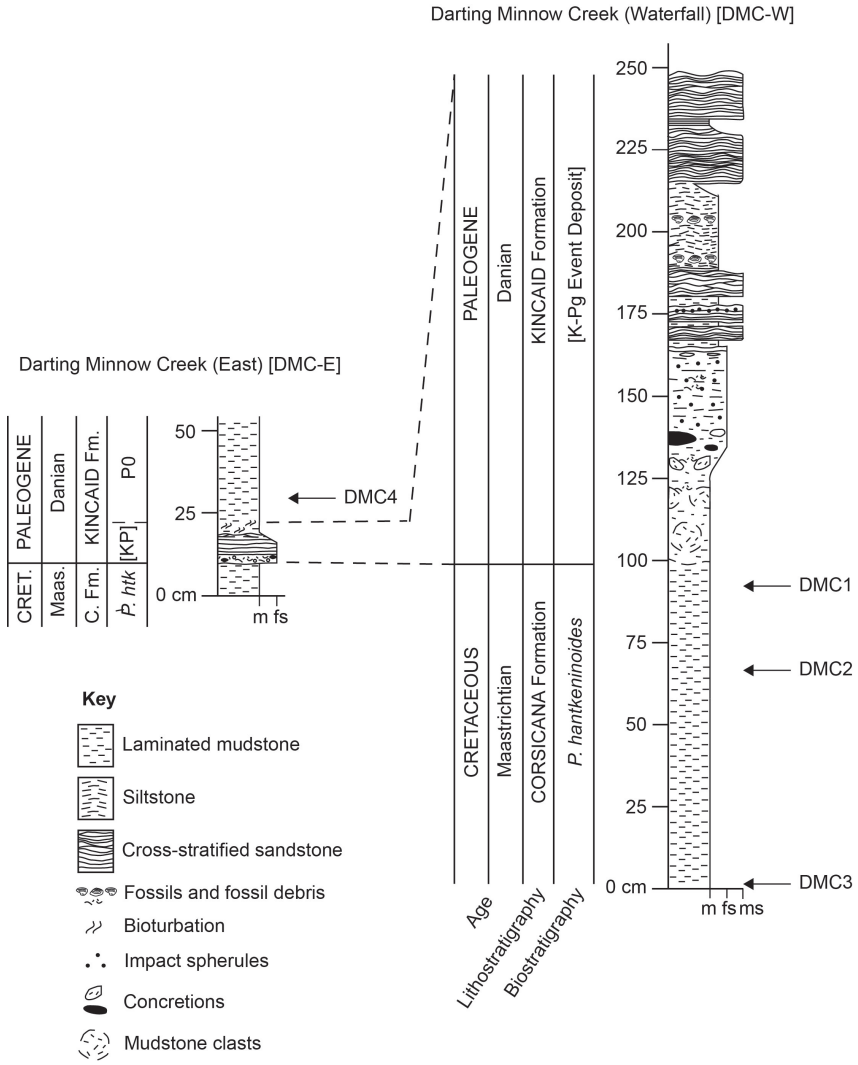

Fig. S2. Stratigraphy and sampling strategy at Darting Minnow Creek, Brazos River, Texas Stratigraphic position of samples measured here (DMC1 - 4) are shown. Log key: m = mud, fs = fine sand, ms = medium sand. Note that samples were taken from within the cross-stratified sandstone units within the K-Pg event deposit at Darting Minnow Creek (Waterfall), but no planktonic foraminifera were recoverable. Position of the K-Pg boundary follows refs. (8, 63). Note extreme variability in thickness of the K-Pg event deposit - the two outcrops are located ∼100 m apart (63).

While the combination of samples from different sites could introduce some external noise to our records, there are a number of reasons to suggest any such noise is not driving our signals. Firstly, at each site pH is calculated from δ^{11}B with pK_B^* estimated according to temperature proxy estimates from the very same material on which the boron isotope measurements are made- therefore regional differences in temperature should not introduce error. Secondly, variability in surface ocean pH was likely very low in the late Maastrichtian, at least in the mid-low latitudes (see Fig. S3). It is therefore highly unlikely that excursions on scales > 0.1 units, as seen at the K-Pg boundary (Fig. 1, main text), could be driven by geospatial variability.

B. Age Models. At ODP Site 1209, we use the astronomical and biostratigraphic tie points from ref. (67) for the Danian, with the exception of the earliest short eccentricity minimum at 261.32 rmcd, which conflicts with the position of their earliest long eccentricity cycle at 261.39 rmcd. In addition, we use the first appearance of *Parvularugoglobigerina eugubina* (marking the base of Pα, 66.0 Ma (68)) appearing at 2cm above the boundary (69). For the Maastrichtian, we use the orbital stratigraphy (Option 3) of ref. (34). In order to maintain across-record consistency with the most recent Geological Time Scale (68), a constant offset was applied to each astronomic model (34, 67) to match a K-Pg datum of 66.04 Ma. Our preferred age model assumes the 40 kyr P0 interval is highly condensed (< 2 cm-thick) but we plot the data in the depth domain here for clarity (Fig. S4).

At Geulhemmerberg Cave, we assign an age of ∼1 kyr after the K-Pg (6, 56, 59); see *Geologie en Mijbouw* 75 (2-3). These authors' interpretation is not without uncertainty (due to for example the absence of a clear Ir layer at this site, and biostratigraphic complexity), but we

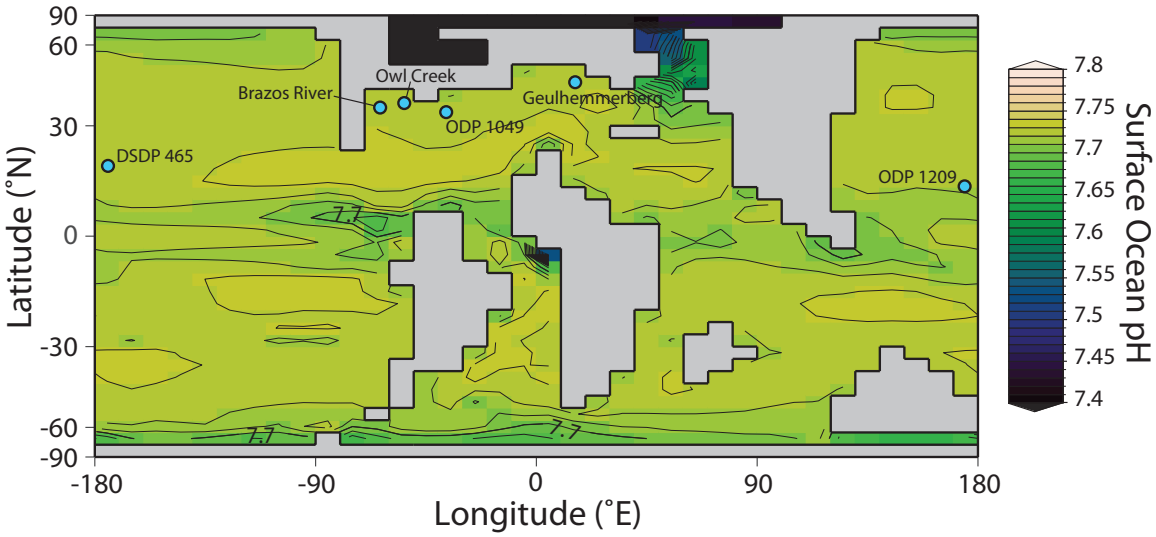

Fig. S3. Simulated Maastrichtian surface ocean pH variability from GENIE. GENIE simulations of Maastrichtian climate (in this example spun up to atmospheric pCO_2 of 850 ppm, see Section A) show very little heterogeneity in mid-latitude surface ocean pH. The variability between our sites (marked in blue) is unlikely to have been greater than a few hundredths of a pH unit, and thus noise added by comparing geographically-disparate sites should be low.

accept their age assignment based on: 1) Sr isotopes in *H. globulosa* indicating they are post-impact in age (56), 2) abundant bryophyte spores in the clay layer (70) that may correlate with the global post-extinction 'fern spike', and 3) the presence of biomarkers that are seen elsewhere immediately after the K-Pg boundary (65). Throughout the Geulhemmerberg section, nannofossil assemblages appear at face value to be later Danian (71), but similarly small specimens of these taxa are found up to 9 m below the K-Pg boundary at Brazos River (Texas), El Kef (Tunisia), and Jebel Qurtasiyyat (Jordan) (72), and in incontrovertibly Maastrichtian strata in the nearby Curfs Quarry (73), indicating these taxa evolved before the K-Pg (72). Conversely, the planktic foraminiferal assemblages in the Geulhemmerberg clay layers almost exclusively comprise *H. globulosa*, a taxon usually considered Cretaceous in age, but that also dominates (up 48 % of the total assemblage) post-impact communities immediately above the K-Pg impact Ir-horizon in New Zealand (74), in finely laminated sediments showing no sign of burrowing or transport (see also ref. (75)). Finally, ammonites are preserved in the nearby Curfs Quarry that are stratigraphically higher than the 'E' clay, which might otherwise suggest a Cretaceous age. Similar Danian ammonites have been found elsewhere, however, suggesting that a number of ammonite species persisted into the Danian (76). Therefore, we accept age assignment of Smit and Brinkhuis, and the interpretation that the absence of all but a trace of an Ir layer in burrows at Geulhemmerberg (77) was due to erosion during high-energy post-impact storm events (6), as is seen elsewhere in northern Europe (78).

Dates for our sample from DSDP Site 465 assume a linear sedimentation rate between the K-Pg boundary and the first appearance of the latest Maastrichtian nannofossil *Micula prinsii*, with positions and ages in the core relative to the K-Pg from ref. (79).

At Owl Creek, dating is approximate, as the ∼10 m section is entirely within the *M. prinsii* zone (7). In the absence of other age constraints, we assign the C30n/C29r boundary to the base of the section (with date from (68)), and assume linear sedimentation rates between this and the contact with Danian sediments. This is an approximation, but the resultant sedimentation rates are comparable with those in nearby sections (7) and as such are probably not unreasonable.

Like Owl Creek, Site ODP 1049 presents some challenges in the construction of a continuous age model over the K-Pg (see refs. (54, 55)). We assign approximate ages to our two samples by extrapolating constant sedimentation rates between the K-Pg boundary (assigned 66.04 Ma (68)) and the midpoint of the depth range given for the base of magnetochron C29r (66.398 Ma; (68)) from ref. (55).

At Brazos River, we measured three samples within the uppermost 1m of the Corsicana Formation below the K-Pg boundary at the section located at Darting Minnow Creek waterfall ("DMC-W"). Insufficient foraminifera were recoverable from the hummocky cross-stratified sandstone layers within the K-Pg event deposit, and we did not sample from finer-grained layers interbedded between the sandstones, from which well-preserved benthic foraminifera have recently been reported (13). We follow the recognition of the K-Pg boundary as in refs. (8, 63), which we note differs from that of ref. (51). Our single sample above the boundary is taken from a stratigraphic interval in the Kincaid Formation 100 m downstream of the waterfall at Darting Minnow Creek ("DMC-E"). Here the K-Pg complex thins to a single ∼10 cm-thick fine sandstone unit. Such complex lateral variability in thickness is probably due to relief on the seafloor, with expanded K-Pg deposits such as are seen at DMC-W filling in topographic lows and thinning onto adjacent highs such as DMC-E (63, 64). Comparison with the placement of a series of early Paleocene marker horizons indicates this early Paleocene sample is stratigraphically contiguous with the biozone P0 described in ref. (8). We therefore assign an approximate age of 20 kyr after the boundary, half-way through the duration of that biozone (68). This approximation assumes that sedimentation rates at Darting Minnow Creek were not constant during P0, but likely increased progressively as carbonate producers recovered from the K-Pg impact. Below the K-Pg boundary, all samples are from planktic foraminiferal biozone CF1, as indicated by the presence of *Plummerita hantkeninoides*. Given a conservative duration for this biozone of 140 kyr (80) and a thickness between the first appearance of *P. hantkeninoides* and the erosive base of the K-Pg event bed in the nearby Mullinax-3 core

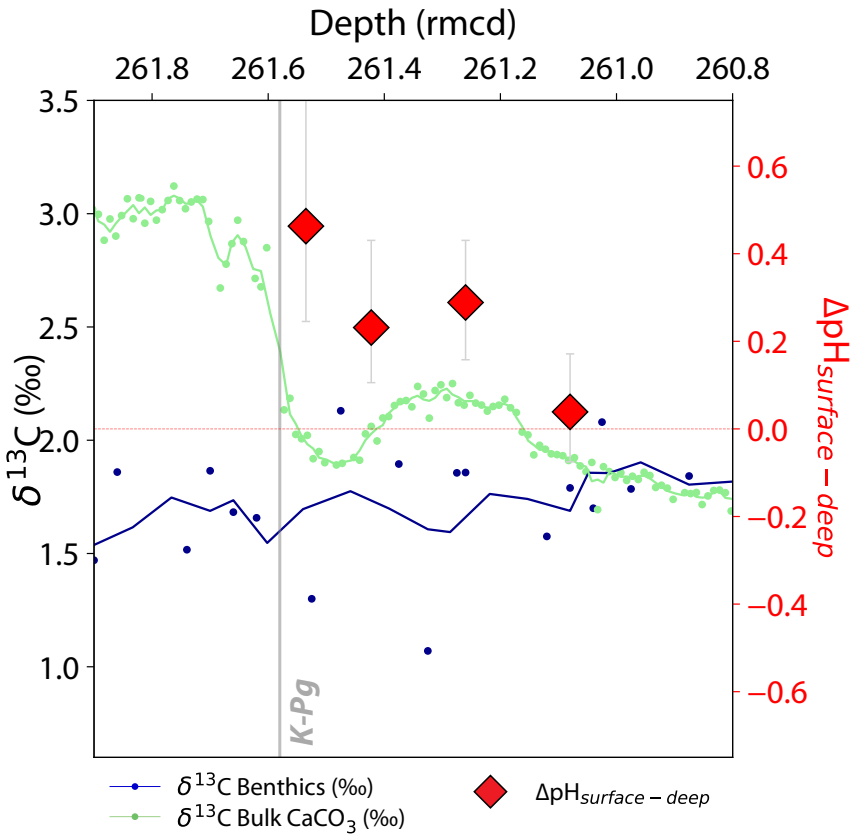

Fig. S4. Planktic-benthic timeslices at ODP Site 1209 vs. depth, in revised metres composite depth (rmcd).

of 2.5 m (51), we assume a late Maastrichtian sedimentation rate of 1.8 cm kyr^{-1}. Although the core site Mullinax-3 nearby has been the subject of Pleistocene alteration (13), the uppermost Maastrichtian biozone CF1 also spans 2.5 m at the Mullinax-1 core taken 3 km north (51). This is significant, because Mullinax-1 is less disturbed, and preserves an event bed similar in thickness to that seen at DMC-W (64), suggesting a similar depositional and topographic setting (i.e. a paleotopographic 'low'). Furthermore, Vellekoop et al. (81) find the first appearance of the dinoflagellate *Manumiella seelandica* (66.1 Ma) at 1 m below the K-Pg event bed at Brazos-1 ($\sim$ 3 km north of DMC). Their resulting sedimentation rate of 1.67 cm kyr^{-1} agrees well with our estimate of 1.8 cm kyr^{-1} assuming a 2.5 m thickness of foraminiferal biozone CF1. Schulte et al. ((82), Table 1) also estimate regional sedimentation rates in the Maastrichtian of "at least 1.25 cm kyr^{-1}", which is also compatible with our age assignment. Elsewhere in the area, a volcanic ash horizon (previously misidentified as a layer of altered impact spherules (51)) is present in the Corsicana Formation $\sim$30 cm below the base of the K-Pg in outcrops along nearby Cottonmouth Creek, 1 km north of our sampling locality. Just as at 'River Bank South' (8) and 'Brazos-1' (81), the ash bed does not outcrop at DMC-W, preventing direct correlation with our samples. This is either because it is not exposed (i.e. it is stratigraphically lower than our exposed section) or it is absent due to either non-deposition, or scouring by seismically-triggered mudflows or tsunami following impact (63, 64). However, a preliminary U-Pb date for this ash of 65.95 Ma (63) is within error of the accepted date of the K-Pg boundary (4, 5, 67), suggesting that if erosion caused its absence at DMC-W, the amount of time missing as a result would be minimal.

C. Species Selection. Species picked for each datapoint are shown in Fig. 1, main text, and listed in the accompanying supplementary Excel file. For benthic foraminiferal samples, we chose exclusively epifaunal taxa, which are thought to record the δ^{11}B of aqueous borate ion faithfully (83). At Site 1209, *Nuttallides truempyi* and *Stensioeina beccariiformis* were used. At shallow shelf sites (Owl Creek and Geulhemmerberg), epifaunal benthic taxa were primarily assigned to the *Cibicidoides alleni-succedens* group, with minor contribution from *Cibicidoides dayi* and *Anomalinoides ?acutus* (see Figs. S5 and S6).

In the case of the planktic foraminifera, to infer atmospheric pCO_2 from boron isotopes it is necessary to analyse foraminifera that grew in the mixed layer, where waters are in communication with the atmosphere. In our shallow water sections, assemblages are largely dominated by *Heterohelix globulosa*, which is consistent with a mixed-layer habitat usually indicated by measurements of oxygen isotopes (at least in well preserved fossil material; (84)). At Owl Creek, the shallow water setting means that only three species of planktic foraminifera were present (*Heterohelix globulosa*, *Hedbergella* sp., and *Rugoglobigerina rugosa*; (42)), and none were abundant enough for boron isotope analysis. However, Geulhemmerberg and Brazos River yielded sufficient planktic foraminifera for analysis. At Geulhemmerberg, the planktic assemblage was comprised almost exclusively of *Heterohelix globulosa*, with little morphological variability (Fig. S7).

At Brazos River, the Maastrichtian assemblage of planktic foraminifera is more diverse than at Owl Creek, including for example

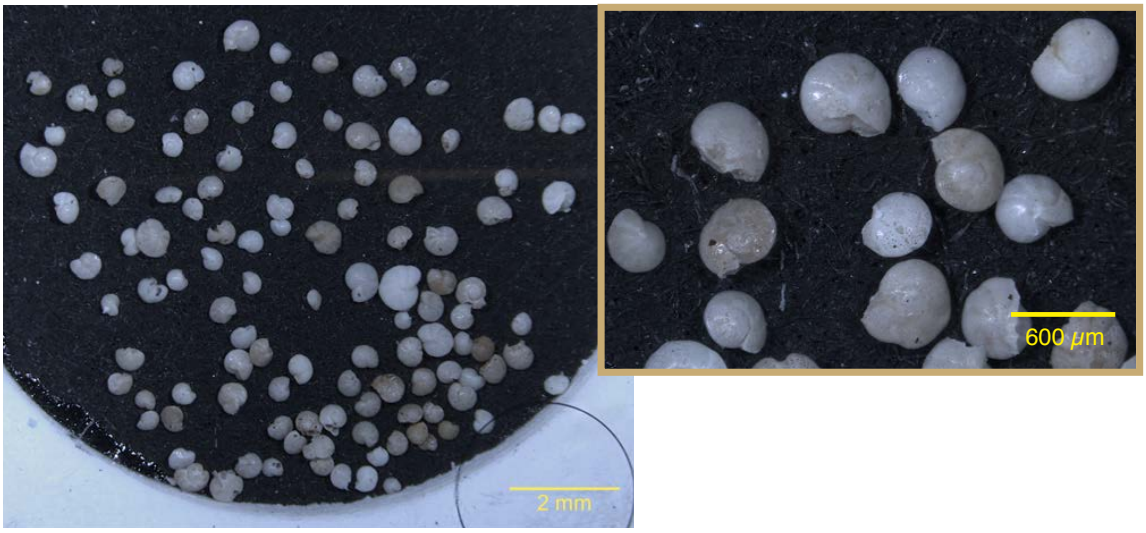

Fig. S5. Epifaunal benthic foraminifera (>212 μm), sampled from Geulhemmerberg Cave. Taxa are predominantly *Cibicidoides alleni-succedens*, with minor contributions from *Cibicidoides dayi* and *Anomalinoides* sp. The sample shown is from the 'E' boundary clay; see e.g. (6). Note, this is only the sample material picked for geochemical analysis from several kg of washed residue, photographed to be transparent about what morphological/preservational range was analysed- this compound-focus light microscope image does not reflect the typical composition of the carbonate sand fraction, and should not be interpreted as abnormally high benthic foraminiferal abundances. A higher resolution image is available on request.

Globotruncana, *Pseudotextularia*, and *Pseudoguembelina*, likely reflecting a somewhat deeper setting. For comprehensive descriptions of planktic assemblages, see e.g. (51, 63, 82). For consistency with Geulhemmerberg, and since it was the most abundant planktic genus, we focussed measurements on *Heterohelix*. However, unlike at Geulhemmerberg, besides *Heterohelix globulosa* a number of morphologically and ecologically similar taxa were present(e.g. *H. striata, H. labellosa*) with a large number of morphologically intermediate specimens (see Fig. S8). Therefore, here we combined these taxa for geochemical analysis as *Heterohelix* sp.

At ODP Site 1049, we analysed *Heterohelix sp.*, so as to be consistent with our shallow water sites (Fig. S9). In addition, we analysed the large Cretaceous planktic species *Contusotruncana contusa* (Fig. S10), for comparison with DSDP Site 465.

In the aftermath of the Cretaceous-Palaeogene boundary at ODP Site 1209, we analyse *Woodringina* sp. *Woodringina hornerstownensis* were dominant in our samples, but we cannot rule out the possible inclusion of some *Woodringina claytonensis*. From some samples, there were also sufficient *Parvularugoglobigerina eugubina* and *Praemurica taurica* to analyse. These species, however, recorded colder temperatures in δ^{18}O and Mg/Ca compared to *Woodringina*, indicating a deeper habitat. As such we can not use these data to calculate surface ocean pH and pCO_2 (plotted in the main text), but the data are included in this study (see accompanying Excel tables) as they can be used to help constrain $\delta^{11}B_{sw}$ (see Section C).

2. Analytical Methods

A. Carbonate Preparation and Analysis. Samples were disaggregated in deionised water, or where necessary (e.g. Brazos River), dilute Sodium Hexametaphosphate solution (2g/L) buffered with NH_4OH, before being dried in an oven at <50 °C. Samples were washed over a 38 μm sieve with deionised water, and dried again at <50 °C. Sample cleaning and preparation for δ^{11}B and trace metal analysis follows refs. (22, 83, 85, 86) and references therein. Briefly, this includes lightly cracking open all chambers and repeated sonication in B-free Milli-Q water (18.2 ΩM) to remove clays, followed by oxidative cleaning (1% H_2O_2 in 0.1 M NH_4OH), and a weak acid leach to remove any potential resorbed contaminants.

Column chemistry and geochemical analyses were primarily carried out at the Yale Metal Geochemistry Center (Yale University), supplemented with data generated at the University of Bristol (UoB). The same protocols were used at each laboratory. Reproducibility of boron isotope measurements across these two laboratories and the University of Southampton has been demonstrated (86, 87) by repeat measurements of a suite of carbonate (JCp-1, JCt-1; (88, 89)) and boric acid (UMD, BIG-D, BIG-E, AE120, AE121, AE122; (90)) standards. Reproducibility of trace element ratio measurements across all three laboratories was verified using in-house synthetic (SECS1, SECS2, SECS3) and carbonate (JCp-1, JCt-1) standards. These standards cover a broad range of B/Ca (30 - 500 μmol/mol) and Mg/Ca (1 - 7 mmol/mol) ratios, more than the range of our samples.

Trace element analysis was carried out using Thermo Element XR (Yale) or Element II (Bristol) ICP-MS. Samples and bracketing standards (in-house synthetic standards BSGS (Bristol) or SMEG (Yale)) were matrix-matched in terms of [Ca]. Long-term reproducibility at each site (2 sd) was better than 5% for B/Ca and Al/Ca measurements, and 3% for Mg/Ca and Sr/Ca. Al/Ca ratios were monitored to verify efficacy of clay cleaning, since the addition of isotopically-light contaminant B from clay may result in artificially light δ^{11}B measurements. Data are listed in the accompanying supplementary Excel file and will be submitted to www.pangaea.de. All samples included in this study bar two below an operational threshold of ~140 μmol/mol commonly used to indicate clay contamination (83). One sample of *H. globulosa* from the critical Geulhemmerberg boundary clay recorded 153 μmol/mol Al/Ca, and as such another sample of clay was washed, picked and analysed from this

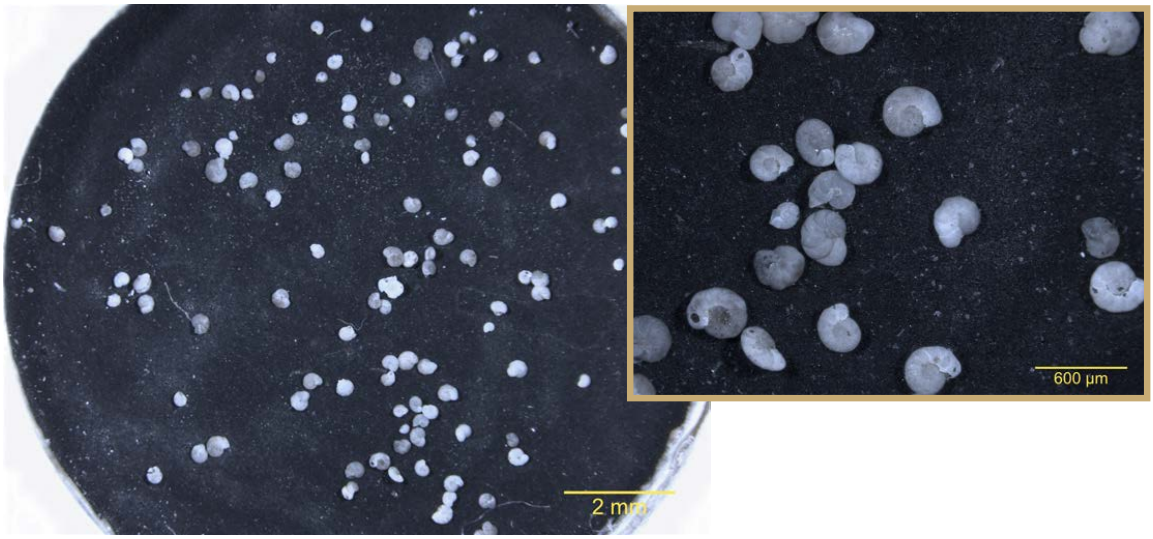

Fig. S6. Epifaunal benthic foraminifera (>212 μm), sampled from Owl Creek. Species picked were predominantly *Cibicidoides alleni-succedens*, with minor contributions from *Cibicidoides dayi* and *Anomalinoides* sp. The sample shown is from 2 m above the section base; see (7, 42). Note, this is only the sample material picked for geochemical analysis, photographed to be transparent about what morphological/preservational range was analysed- this compound-focus light microscope image does not reflect the full benthic foraminiferal assemblage; for details as to benthic assemblages, see e.g. (42). A higher resolution image is available on request.

interval. This repeat sample yielded B/Ca, Mg/Ca and δ^{11}B values indistinguishable from the first, despite lower Al/Ca (23 μmol/mol). We therefore concluded that the high Al/Ca in our first replicate did not introduce error. Another sample from Owl Creek also displayed high Al/Ca (1.2 mmol/mol), but since it is not anomalously low in δ^{11}B compared to contemporaneous measurements, we do not exclude it.

Boron isotope analyses were carried out on Thermo Neptune Multi-Collector ICP-MS, equipped with 10^{11} (UoB) or 10^{12} Ω amplifiers (Yale). External reproducibility was estimated from repeat measurements of carbonate standard JCp-1, using relationships between 11B signal intensity (primarily dictated by sample size) and long-term reproducibility at the UoB (83) and Yale (86).

For boron samples, a subsample of crushed, cleaned and homogenised $CaCO_3$ was taken where sample size permitted for δ^{13}C and δ^{18}O analysis on a Thermo-Finnigan MAT 253 mass spectrometer coupled to a Kiel Device at Yale Analytical and Stable Isotope Centre (YASIC) (see Supplementary Excel File). All isotope values are reported in ‰ relative to the Vienna Peedee belemnite standard (VPDB). Analytical precision of replicates of standard measurements is typically better than 0.06 and 0.08 ä for carbon and oxygen, respectively. In addition, we include (see Supplementary Excel File) new bulk and benthic foraminiferal $CaCO_3$ δ^{13}C measurements from ODP Site 1209 (Fig. 2a, main text). The bulk carbonate record and some of the new benthic foraminiferal data were generated with a Thermo-Finnigan MAT 253 mass spectrometer coupled to a Kiel Device at the University of California Santa Cruz, a lab with analytical precision (1σ) of $\pm$ 0.05 ‰ for δ^{13}C and $\pm$ 0.08 ‰ for δ^{18}O based on repeated analyses of in-house standards. The boundary portion of this bulk carbonate record has been published in part (91), but the data is provided here for the first time. Other benthic foraminiferal data was generated at the Scripps Institution of Oceanography using a Carousel-48 automatic carbonate preparation device and a common acid bath (i.e., a Fairbanks device) coupled to a Finnigan MAT 252 mass spectrometer, with an analytical precision (1σ) of $\pm$ 0.04 ‰ for δ^{13}C measurements.

B. Organic Geochemistry. Organic temperature proxies from Geulhemmerberg were used to verify our Mg/Ca-based temperature reconstructions (see Section 4), and measured at Yale University. A sample of the clay was freeze-dried and homogenised with a mortar and pestle. Lipids were extracted from ~10 g of dry sediment using a Dionex 300 Accelerated Solvent Extractor using a solvent mixture of dichloromethane:methanol (2:1, v/v). The resulting total lipid extract was then passed through a silica gel column to separate apolar, ketone and polar fractions using hexane, dichloromethane and methanol, respectively. Polar fractions were then further purified by passage through activated basic alumina gel using a solvent mixture of dicholoromethane/methanol (1:1; v/v) following (92). After being dried under a stream of nitrogen, the polar fraction was re-dissolved in hexane/2-propanol (99:1; v/v) and passed through a 0.45 μm PTFE filter. Isoprenoidal and branched glycerol dialkyl glycerol tetraethers (GDGTs) were analysed using the filtered polar fraction with an Agilent 12 high performance liquid chromatograph (HPLC) system coupled to a 6130 quadrupole mass selective detector (MSD). Compounds were separated using two UHPLC silica columns (BEH HILIC columns, 2.1 $\times$ 150 mm, 1.7 μm; Waters) in series, fitted with a Waters 2.1 $\times$ 5 mm silica pre-column of the same material and located in a column compartment maintained at 30 °C (93). The sample was eluted isocratically for 25 minutes with hexane/2-propanol (98.2:1.8; v/v), followed by a linear gradient to hexane/2-propanol (96.5:3.5; v/v) for 25 minutes, and then a linear gradient to hexane/2-propanol (90:10; v/v) over 30 minutes that was then maintained for 10 minutes. Flow rate was 0.2 ml/min and back pressure ranged from 195 to 210 bars. Total run time was 110 minutes, including 20 minutes for re-equilibration. GDGTs were detected using selective ion monitoring of the protonated molecules [M+H]+, with Atmospheric Pressure Chemical Ionisation (APCI) source conditions as in (92).

Isoprenoidal GDGTs were used to construct the TEX_{86} index (94), which was used to estimate mean annual sea surface temperature (SST) using the TEX_{86}^{H} calibration (95). The root mean square error (RMSE) of the TEX_{86} SST estimate is ~2.5 °C. Branched GDGTs, assumed to derive from soil organic matter, were used to construct the MBT'5ME index following (96) and converted to mean annual terrestrial air

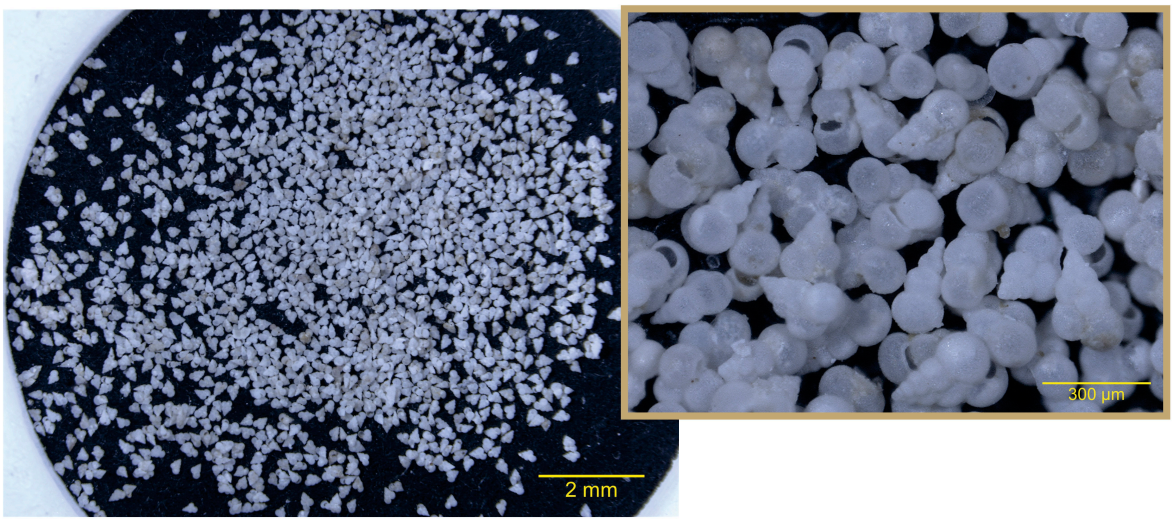

Fig. S7. ***Heterohelix globulosa*** **(150-212 μm), sampled from Geulhemmerberg Cave** 'E' boundary clay; see e.g. (6). Note, this is only the sample material picked for geochemical analysis, photographed to be transparent about what morphological/preservational range was analysed- this compound-focus light microscope image does not reflect the typical composition of the carbonate sand fraction. A higher resolution image is available on request.

temperature using the calibration of (97). The MBT'5ME temperature estimates has a RMSE of ∼4.5 °C.

3. Vital effects and species cross-calibration

While foraminiferal carbonates consistently show relationships between δ^{11}B and ambient pH (e.g. refs.(87, 98)), their boron isotope compositions often differ from those predicted for ambient seawater $B(OH)_4^-$ ion. These offsets are commonly attributed to various physiological processes of the foraminifera imprinting on their geochemical signatures- so called 'vital effects' (see e.g. (99)). In the case of our benthic foraminifera, because we measured epifaunal taxa, our measurements should reflect bottom water conditions without any vital effect, and without bias from porewater chemistry (83). However, the δ^{11}B of almost all planktic foraminifera alive today is offset from seawater $B(OH)_4^-$ ion to some degree (99), and thus the assumption that $\delta^{11}B_{foram} = \delta^{11}B_{B(OH)_4^-}$ is probably invalid for at least some of our Cretaceous-Palaeogene planktic foraminifera. We therefore attempted to infer vital effects based on what is known about the ecophysiology of these extinct taxa, by analogy with modern species.

H. globulosa usually, although not exclusively (48, 100), displays signatures of a shallow, mixed layer depth habitat (e.g. (84, 101, 102)). Its relatively steep increase in δ^{13}C with size could indicate the presence of photosynthetic symbiosis (e.g. (101, 103) and references within), but this by no means certain (101). Uncertainty as to its ecology thus precludes a straightforward application of an analogous modern calibration. Instead we quantify a vital effect in *H. globulosa* by comparison with epifaunal benthic foraminifera that grew in the mixed layer alongside *H. globulosa* at Geulhemmerberg. Since these symbiont-barren epifaunal benthics should not display a vital effect (83), we can assume that any offset in pH calculated from *H. globulosa* is due to physiological interferences (e.g. microenvironmental alteration; (99)). We observed a pH offset in *H. globulosa* of ∼-0.2 units relative to co-occurring benthic foraminifera, which is most similar to vital effects seen in symbiont-barren species such as *Globigerina bulloides* today (104). This would therefore be hard to reconcile with the presence of dinoflagellate symbionts in this taxon, as has previously been suggested (103). We adjust pH measurements from *H. globulosa* elsewhere to account for this vital effect.

Contusotruncana contusa at ODP Site 1049 can record δ^{18}O values similar to, or even lighter than, species that are widely recognised as shallow mixed layer dwellers, such as *R. rugosa* (e.g. (100, 105)). It has also been posited as potentially harbouring photosynthetic symbionts (106). However, we observe no offset in δ^{11}B between *C. contusa* and *H. globulosa* measured in the same sample (see accompanying Excel file), and therefore we apply the vital effect correction for *H. globulosa* to *C. contusa*.

While we have no direct means to cross-calibrate the Danian planktic genus *Woodringina* to cohabiting benthics, we suggest its vital effects may be similar to those seen in *H. globulosa* of the same size. *Woodringina* displays a similar gradient of δ^{13}C with test size as *H. globulosa* (101), both species have very similar morphologies (e.g. see Figs. S7 and S11), and oxygen isotopes in both species appear to suggest a mixed layer habitat (27, 84). Therefore we again apply the vital effect derived for *H. globulosa* to *Woodringina*.

Although more work is required to fully decipher Cretaceous foraminiferal vital effects, we stress that the main findings of our study are not dependent on choice of species or vital effect. At Geulhemmerberg, δ^{11}B values of *H. globulosa* in the aftermath of impact are lighter (suggesting lower pH) than in any preceding Cretaceous sample of the same species and size fraction. Similarly, our planktic-benthic pairs always used *Woodringina sp.* vs. epifaunal benthics, so the structure of vertical pH gradient change in the early Danian is independent of any vital effect.

4. Mg/Ca temperature calculations

Because not all of our sites yielded 'glassy' (57) foraminifera, oxygen isotope-derived temperatures from our foraminifera would likely be underestimates of *in situ* growth temperature (due to early-stage diagenetic recrystallisation, (57)). While not immune to diagenetic alteration

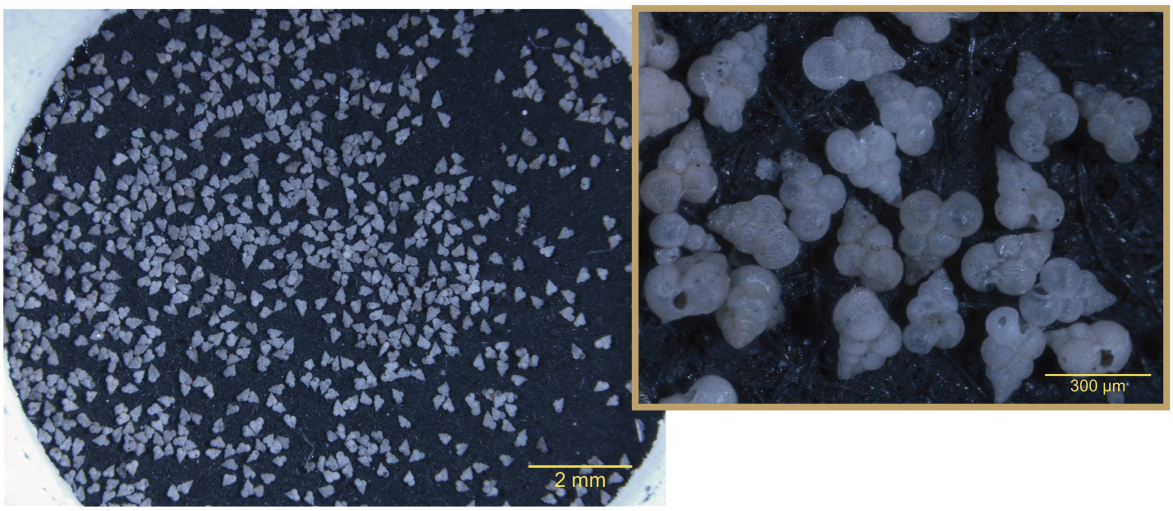

Fig. S8. *Heterohelix sp.* (150-212 μm), sampled from Darting Minnow Creek, Brazos River. The sample shown here is 'DMC2', 20-30cm before the boundary. Note, this is only the sample material picked for geochemical analysis, photographed to be transparent about what morphological/preservational range was analysed- this compound-focus light microscope image does not reflect the assemblage at Brazos as a whole; for details of the broader assemblage, see e.g. (51, 63, 82). A higher resolution image is available on request.

(66), Mg/Ca-derived temperatures are less susceptible to this resetting. Therefore, we used planktic foraminiferal Mg/Ca, measured on an aliquot of each δ^{11}B sample, to estimate sea surface temperature (and hence allow us to calculate pH and pCO_2 accurately from δ^{11}B). Modern Mg/Ca-temperature calibrations cannot be directly applied to the K-Pg, however, because of the different Mg/Ca$_{sw}$ and background ocean pH at this time.

Here we assume Ca concentrations in the K-Pg ocean of 21 mMol, through linear interpolation of reconstructions of refs. (107) and (108), and a [Mg] of 42 mMol given a Mg/Ca$_{sw}$ ratio of 2 (from ref. (109)). We therefore attempted to calculate temperature accounting for the non-linear response of foraminiferal Mg/Ca to changing Mg/Ca$_{sw}$ following ref. (110). However, Evans et al. (110) found that 6 of 20 different possible least squares models of the Mg/Ca$_{sw}$-Mg/Ca$_{test}$ relationships deviated from their empirical culture calibrations by less than 0.1 mmol/mol Mg/Ca, with marginal differences in goodness-of-fit between the models. The divergences of those 6 models between a Pliocene-present range of Mg/Ca$_{sw}$ of 3.4 - 5 mmol/mol was minimal, but they diverge strongly at a Maastrichtian Mg/Ca$_{sw}$ of 2.

To address this source of uncertainty, we use our sample from Geulhemmerberg, where foraminiferal preservation was glassy, and organic temperature proxies could also be measured (see Section B), to test which of ref. (110)'s possible model fits results in the best fit for a Cretaceous Mg/Ca$_{sw}$ of 2. Assuming a palaeolatitude correction (111) for 45 °N, with an ice-free value of $\delta^{18}O_{sw}$ of -0.89 (112), oxygen isotopes in planktic *H. globulosa* and benthic *Cibicidoides* gave temperatures of 22 °C and 20.7 °C respectively. TEX$_{86}$ measured in the same clay layer gave a mean-annual sea surface temperature of 23.4 ± 2.5 °C (using the TEX$_H$ calibration of ref. (95)), while MBT'5ME measurements from terrestrially-derived compounds suggest mean annual soil temperatures of 23 .0 ± 4.5 °C (using the equation from ref. (97)). This reasonable agreement between oxygen isotopes and organic temperature proxies contrasts with Mg/Ca-based sea surface temperature values of 30.7 °C using Evans et al. (110)'s preferred model, where both A and B in the general Mg/Ca-Temperature calibration (Eq. Eq. (1)) are both related to Mg/Ca$_{sw}$ via quadratic functions.

$$\text{Mg/Ca}_{\text{test}} = \text{B}exp^{\text{AT}} \quad [1]$$

This overestimate is not due to the application of a pH correction: not correcting for low pH would make this temperature even higher. It is also unlikely to be a result of an incorrect assignment of Mg/Ca$_{sw}$ for the K-Pg, since benthic foraminiferal Mg/Ca temperatures using the calibration of Lear et al. (113) and an 'H' value of 0.51 to account for Mg/Ca$_{sw}$ sensitivity in benthic foraminifera (as estimated for *Oridorsalis umbonatus* by Evans et al. (110)) agree well with δ^{18}O temperatures. Therefore we suggest that the preferred least squares model from ref. (110), while a marginally better fit for their calibration at 3.4 mmol mol^{-1}, may not be optimal for lower, Cretaceous Mg/Ca$_{sw}$.

Of the six other model fits that Evans et al. (110) agreeing within an average of 0.1 mmol/mol Mg/Ca of their empirical culture calibrations, we find the best fit with TEX$_{86}$ data from Geulhemmerberg (~3°C better) to be a quadratic fit for the relationship between B and Mg/Ca$_{sw}$ with an intercept of 0, and a linear fit between A and Mg/Ca$_{sw}$ (see Eq. 2 below).

$$\begin{aligned} B &= -0.0147 \times (\text{Mg/Ca}_{\text{sw}})^2 + 0.169888 \times (\text{Mg/Ca}_{\text{sw}}) \\ A &= 0.002677 \times (\text{Mg/Ca}_{\text{sw}})^2 + 0.07047 \end{aligned} \quad [2]$$

We therefore use this to generate temperature estimates from planktic foraminiferal Mg/Ca.

Additionally, there is a (sizeable) effect of pH on foraminiferal Mg/Ca (e.g. ref. (114)), and surface ocean pH in the latest Cretaceous was considerably lower than today. Since pH calculations require temperature estimates (in order to calculate pK_B^*), pH corrections on Mg/Ca-derived temperatures are more complex. We therefore iteratively correct both parameters: first calculating pH for a given Mg/Ca-derived

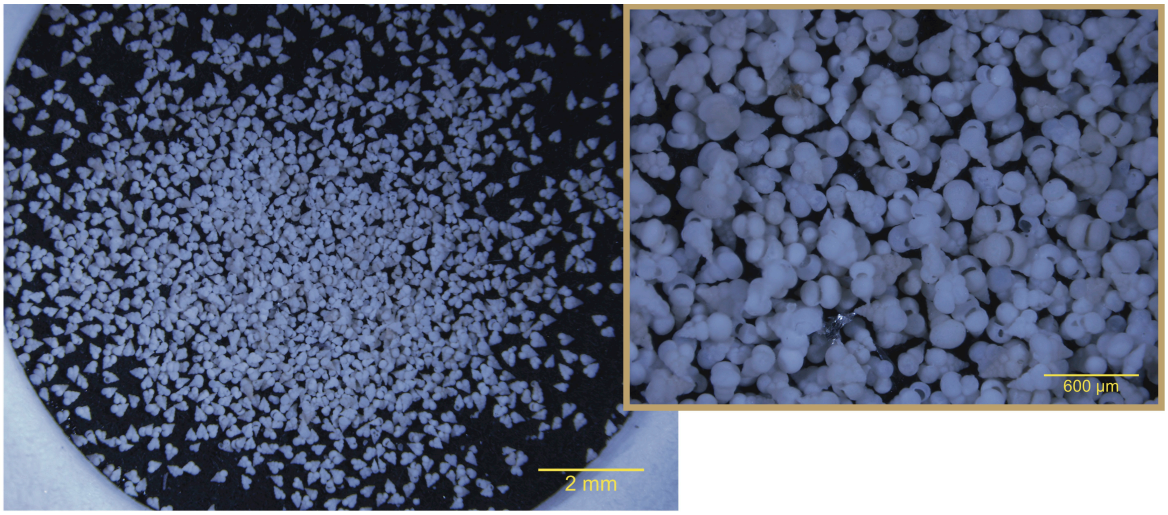

Fig. S9. *Heterohelix sp.* (150-212 μm), sampled from ODP Site 1049. Sample shown here is from 1049C, 9X3, 12-14.5cm. Note, this is only the sample material picked for geochemical analysis, photographed to be transparent about what morphological/preservational range was analysed- this compound-focus light microscope image does not reflect the assemblage as a whole; for details of the broader assemblage, see e.g. (55). A higher resolution image is available on request.

temperature and equilibrium constants, then correcting Mg/Ca temperatures for pH according to the linear fit of (114) (Eq. 3), and so on until values converge (typically within 0.002 pH units in 4-5 iterations).

$$\text{Mg/Ca}_{overestimate} = (-0.7 \times \text{pH}) + 6.7 \quad [3]$$

There are uncertainties associated with this approach, but the alternative of using potentially spurious cold temperatures from δ^{18}O in non-glassily preserved foraminifera for pH and pCO_2 calculations would introduce anomalies within our time-series that stem from differential microfossil preservation. An extension of the sorts of experiments from ref.(110) across different species and lower Mg/Ca_{sw} would undoubtedly be desirable, but our approach can be considered a best approximation at this time. Our Mg/Ca temperature reconstructions (unlike our tropical δ^{18}O temperatures) agree reasonably well with tropical sea surface temperatures simulated by GENIE for the late Maastrichtian (30-32 °C). Our Mg/Ca-derived temperatures at Brazos River, also, range from 31-33 °C, closely matching TEX_{86} derived temperatures of 30-32 °C for these same intervals at Brazos River (81).

5. Calculations

All calculations were carried out using R (115), with specifics described in the following subsections.

A. Boron and Carbonate Speciation Calculations. Boron and carbonate speciation calculations use temperatures from each site as discussed in section 4, and salinities for each site taken from our control Maastrichtian GENIE simulation (for full details see Section A). Given the very different major ion composition of seawater (in particular [Ca] and [Mg]; e.g. (108)) in the late Cretaceous, and the potential for this to introduce significant bias in carbonate system calculations (116), here we use K_w, K_0, K_1, K_2, K_B, $K_{SO_4^{2-}}$ and $K_{SpCalcite}$ constants from MyAMI (116). These constants are calculated for a K-Pg ocean of [Ca] 21 mMol and [Mg] 42 mMol ((107–109); see Section 4 above). Additionally, the ocean in the Cretaceous likely had a lower total [B], so we assume a seawater [B] of 4.1 ppm following ref. (117).

All equilibrium dK constants for the boron and carbonate systems were adjusted for pressure differences (e.g. between benthic and planktic foraminifera) following Millero (118), using the values given in (119). Estimated palaeodepths in metres for each site (Table S1) were converted to pressure in bars via Eq. 4 below.

$$\text{Pressure}_{bars} = \text{Depth}_m \times 0.100693064 \quad [4]$$

Boron calculations from δ^{11}B, and subsequent carbonate system calculations (e.g. pCO_2, etc.) were calculated using the equations in Zeebe and Wolf-Gladrow (120), using the K constants outlined above. As discussed in Sections 3 and 4, we derive the pH offset between *Heterohelix globulosa* and epifaunal benthic foraminifera at Geulhemmerberg, and take this to be the microenvironment acidification in these symbiont-barren foraminifera (see (99)). This vital effect offset can then be applied to analogous species of foraminifera, to derive ambient seawater pH. Mg/Ca-derived temperatures are then corrected for pH (see Section 4), then these temperatures used to derive pK_B^* and pH, until values converge (3-5 iterations). We note that the observation of a flattened vertical pH gradient in the ocean shown in Fig. 2a, main text is apparent even in raw δ^{11}B and δ^{18}O values, without any of the corollary information that must be input to calculate pH from δ^{11}B (see Fig. S12).

B. Second Carbonate System Parameter. To calculate [DIC], pCO_2 and $\Omega_{Calcite}$, a second carbonate system parameter (besides pH) is required. We use estimated Total Alkalinity (TAlk), as calculations are relatively insensitive to this parameter (e.g. (87, 121)). We estimate TAlk prior to the onset of Deccan Volcanism using our late Maastrichtian GENIE simulations (see Section A below), with reference to each

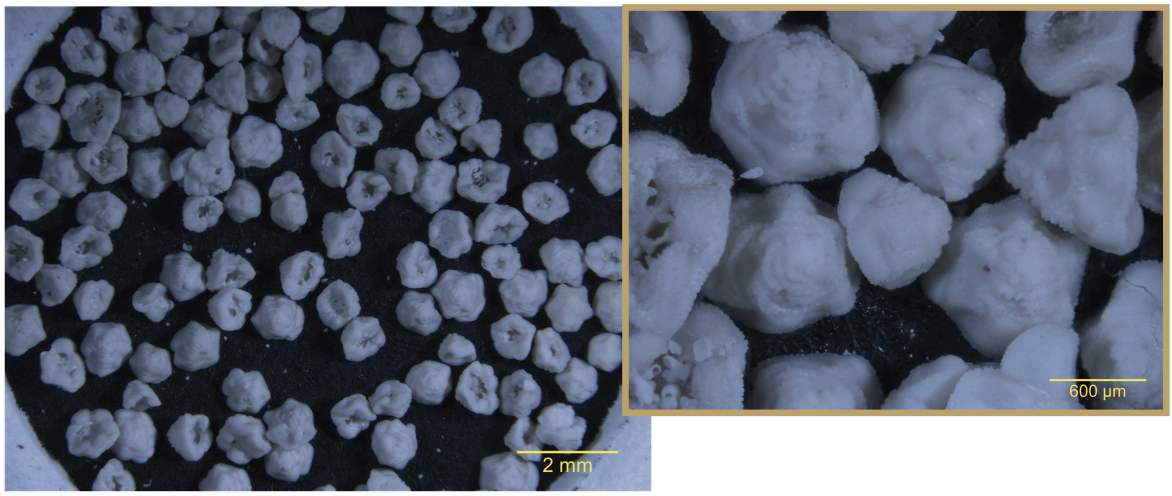

Fig. S10. ***Contusotruncana contusa*** **(355-425 μm), sampled from ODP Site 1049.** Sample shown here is from 1049C, 9X3, 12-14.5cm. Note, this is only the sample material picked for geochemical analysis, photographed to be transparent about what morphological/preservational range was analysed- this compound-focus light microscope image does not reflect the assemblage as a whole; for details of the broader assemblage, see e.g. (55). A higher resolution image is available on request.

site's geographical location and water depth. However, since ocean alkalinity was likely highly dynamic around the K-Pg event, with changes driven by volcanic degassing, subsequent silicate weathering and CO_2 drawdown, and elimination of calcifying organisms (22), we cannot assume this model-derived alkalinity can be applied across our entire record. For this reason, we use published LOSCAR simulations from ref. (22) that approximately match observed carbonate compensation depth (CCD) and temperature changes for each ocean basin around the K-Pg. Specifically, for each ocean box in LOSCAR (see ref. (122)) we obtained trajectories in alkalinity over the K-Pg, and apply this relative shift in alkalinity (see Fig. S13) to our baseline GENIE-derived Maastrichtian values at each site, in accordance with the age of the sample.

We stress that while this is likely a more accurate estimate of alkalinity than not considering spatial or temporal variability, the choice of alkalinity value is not critical to the interpretation of our pCO_2 data. In Fig. S14, our preferred scenario is compared to calculations using a constant alkalinity of 2000 μmol kg^{-1} throughout, illustrating that the choice of secondary parameter does not drive our patterns.

C. The Boron Isotopic Composition of Seawater, $\delta^{11}B_{sw}$. A necessary prerequisite (besides estimated pK_B^*) for calculating pH from $\delta^{11}B_{CaCO_3}$ is the bulk boron isotope composition of seawater. The residence time of the boron isotope composition of seawater is thought to be 10-20 Myr (117, 123, 124), and so it is not permissible to use the modern value of 39.61 ‰(125) in deep time reconstructions. We use approaches used elsewhere (126) to constrain $\delta^{11}B_{sw}$; namely judging the feasibility of apparent oxygen utilisation (AOU) and oceanic carbonate saturation state (Ω_{calcite}) produced by a given $\delta^{11}B_{sw}$ (results given in TableS2).

The AOU approach (126, 127) works via calculating the offset in dissolved inorganic carbon (DIC) between surface and deeper-dwelling foraminifera predicted by δ^{11}B-derived pH (given estimated alkalinity) at a given $\delta^{11}B_{sw}$. Since an increase in DIC with depth arises from respiration of sinking organic matter, a given increase in DIC corresponds stoichiometrically to a given consumption of oxygen. By calculating the maximum theoretical [O_2] at the surface, given reconstructed temperature and assumed salinity (and using the equations from ref. (128) and references therein), and applying the surface-mid-depth gradient in O_2 inferred from DIC, one can infer the maximum O_2 at depth. If the habitat of the deeper-dwelling foraminifera is lower in [O_2] than the lowest known tolerance of [O_2] in modern planktic foraminifera (44.7 μmol kg^{-1}; (129)), it may be concluded that such a high $\delta^{11}B_{sw}$ (and hence DIC gradient) is not feasible. Amongst our data, two Danian time-slices (comparing deep-dwelling *Parvularugoglobigerina eugubina* to shallow-dwelling *Woodringina*) allow us to demonstrate that above a $\delta^{11}B_{sw}$ of 39.85 ‰, DIC gradients would produce maximum [O_2] at the depth of *P. eugubina* that was likely too low for survival (see TableS2).

The foundation of saturation-based constraints is that the surface ocean (at least since the advent of pelagic calcifiers) typically has inherent limitations to what saturation state is feasible. If saturation is too high, there will be enhanced burial of carbonate and/or localised abiotic precipitation to bring it back down, while if too low, deep sea saturation would correspondingly be so low as to prompt carbonate dissolution and hence buffering (see refs. (130, 131)). The use of Ω_{calcite} as a constraint on K-Pg $\delta^{11}B_{sw}$is aided by the fact that there were large changes in δ^{11}B measurable over a geologically short interval, and by our combination of deep-sea benthic and planktic foraminifera in this record. In agreement with the AOU approach outlined above, $\delta^{11}B_{sw}$ of >39.85 ‰ (or 40.15 ‰ at 95 % confidence) will produce $\Omega_{\text{calcite}} < 1$ for some of our sites, which cannot be possible given we recovered plentiful undissolved and unfragmented foraminifera (see e.g. Figs S7, S9). It can also be assumed that ocean saturations of > 10 cannot be sustained over prolonged periods, due to the enhancement of deep-sea carbonate burial, and the likely precipitation of abiogenic carbonate (130). We find that Eocene-like values of $\delta^{11}B_{sw}$ (126) produce unrealistically high vales of Ω_{calcite}: in our lowermost Danian *Woodringina* time-slice the median of 1,000 Monte Carlo simulations of Ω_{calcite} would surpass 15. Below a $\delta^{11}B_{sw}$ of 38.75 ‰, at least two samples of Danian *Woodringina* produce Ω_{calcite} of >10 in over 95% of their Monte Carlo simulations. This would require seawater Ω_{calcite} to remain above 10 for more than 11 kyr, something that is hard to envisage (130). That said, δ^{11}B in our earliest Danian *Woodringina* produces an Ω_{calcite} of >10 at 95% confidence (Fig. S15) even up to values of $\delta^{11}B_{sw}$ that are incompatibly high for other reasons (see TableS2). This implies that oversaturation in the post-impact ocean, in the aftermath of the extinction of calcifiers, was

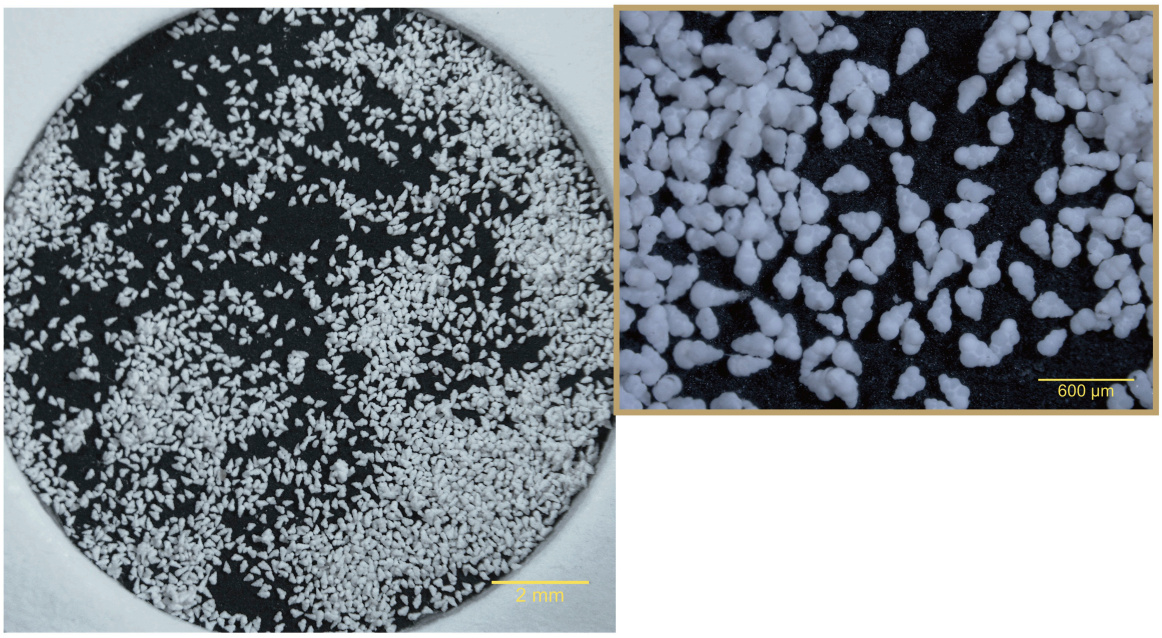

Fig. S11. *Woodringina* sp. (125-150 μm), sampled from ODP Site 1209, Hole A, 25H6, 108-110 cm. Note, this is only the sample material picked for geochemical analysis, photographed to be transparent about what morphological/preservational range was analysed- this compound-focus light microscope image does not reflect the assemblage as a whole; for details of the broader assemblage, see e.g. (69). A higher resolution image is available on request.

so high as to at least briefly exceed 10 at its peak- consistent with the intervals of anomalous carbonate preservation in previously sub-lysocline settings (132, 133), and evidence for abiotic carbonate precipitation (32), as response mechanisms to this imbalance (see (22, 30)).

Besides these extreme end-members, under 'normal' Cretan Ocean functionality, the feasible range of possible surface ocean Ω_{calcite} is limited (see refs. (130, 131)). Thus we can use the δ^{11}B of pre-event Maastrichtian surface-dwelling foraminifera as a further constraint on $\delta^{11}B_{sw}$. For the purposes of estimating Eocene $\delta^{11}B_{sw}$, Anagnostou et al. (126) defined a feasible range of Eocene surface Ω_{calcite} of 5.5 - 7.5. Here we allow surface saturation to drop to 5, since our GENIE simulations suggest latest Maastrichtian open-ocean surface saturation could have reached such values regionally (although probably not at our sample sites; see Fig. S16). At $\delta^{11}B_{sw}$ of <39.05 ‰, Maastrichtian surface ocean Ω_{calcite} estimates would exceed 7.5 at 95% confidence. Conversely, at or above 39.85 ‰, our epifaunal benthic foraminifera at the shallow-water site Owl Creek produce $\Omega_{\text{calcite}} < 5$. We make a distinction in TableS2 between Maastrichtian samples from within magnetochron C29r and those within C30n. This is to distinguish those samples where Deccan emplacement after the C29r/C30n could theoretically have played a role in lowering surface ocean saturation, and those that could not have been subject to any volcanic influence. However, given the timescales of Deccan eruptions (emplacement over 100s of kyr, (134–136)), it is extremely unlikely that volcanic degassing could have dramatically outpaced carbonate compensation by deep sea carbonate dissolution and reduced surface ocean Ω_{calcite} to below 5 at our sites (22, 137).

Combining these constraints, we obtain a range of plausible $\delta^{11}B_{sw}$ for the K-Pg interval of 39.05 - 39.85 ‰. These values are slightly higher than those reconstructed by (138) for the Paleocene-Eocene Thermal Maximum (38.9 $\pm$ 0.4 ‰), only $\sim$ 10 Myr later. However the lower [B] in the Cretaceous-Palaeogene ocean means that the residence time of B in the ocean at this time may have been somewhat lower than the 14 Myr estimated today (117), so this is not unreasonable. Note the timespan of our record is short ($\sim$1 Myr) compared to any estimate of residence time of boron, and so it can be assumed that $\delta^{11}B_{sw}$ remains constant over the studied interval. Although $\delta^{7}Li_{sw}$ appears to drop precipitously at the K-Pg boundary (139), and both the main causes of fractionation in the earth system (e.g. sorption to secondary minerals) and the evolution in the seawater composition of Li and B isotopes are similar, we do not advocate a similar drop in $\delta^{11}B_{sw}$. Firstly, the residence time of B in seawater is far greater than that of Li (124). Secondly, the fact that this drop in $\delta^{7}Li_{sw}$ as recorded in carbonates does not appear to be borne out in records from marine clays (140) suggest that this may be an artefact of either changing lithium isotope vital effects in post-extinction foraminiferal assemblages, or some other non-seawater control on carbonate $\delta^{7}Li_{sw}$ (e.g. pH; (141)). Finally, if $\delta^{11}B_{sw}$ did behave like $\delta^{7}Li_{sw}$ over the K-Pg boundary, it would make the high $\delta^{11}B_{CaCO_3}$ values we observe in the earliest Danian even harder to explain: a lower $\delta^{11}B_{sw}$ would produce unfeasibly high ocean saturation states (TableS2). Therefore, while we encourage further investigations into changes in seawater isotope composition over the K-Pg, they are not driving the patterns we see here.

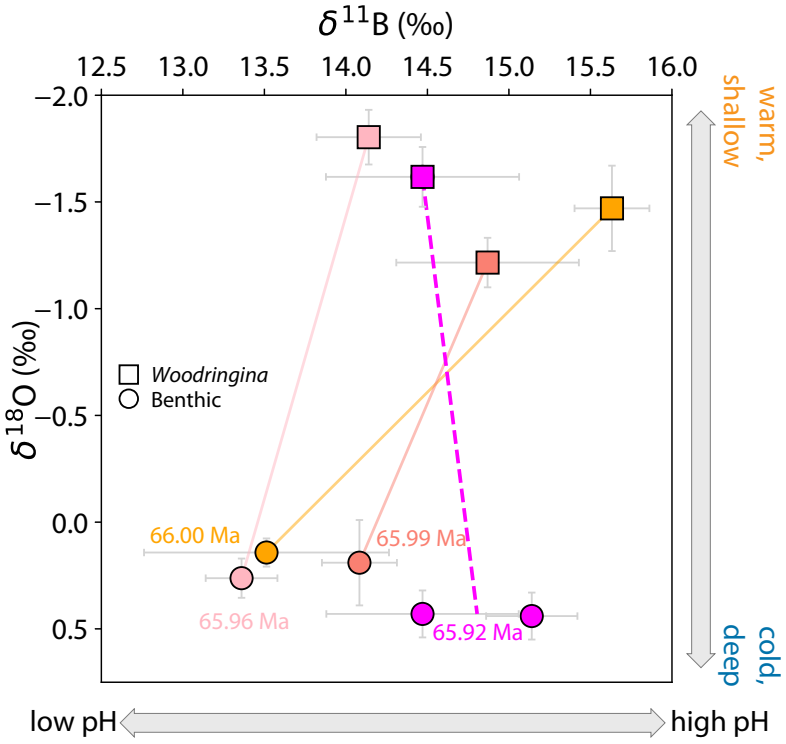

Fig. S12. Reversed pH gradients at ODP Site 1209 apparent in raw δ^{11}B. Today, surface-dwelling planktic foraminifera live in warmer temperatures and higher pH waters than benthic foraminifera (who live in colder, lower pH waters), and thus record heavier δ^{11}B and lighter δ^{18}O. This vertical pH gradient comes from the uptake and export of carbon from the surface ocean as organic matter, and the remineralisation of this organic carbon at depth, via the 'biological pump'. Even without any further pH calculations, changes in this biological pump are apparent at our latest time-slice (in magenta) in raw δ^{11}B.

Michael J. Henehan*, Andy Ridgwell, Ellen Thomas, Shuang Zhang, Laia Alegret, Daniela N. Schmidt, James W. B. Rae, James D. Witts, Neil H. Landman, Sarah E. Greene, Brian T. Huber, James Super, Noah J. Planavsky and Pincelli M. Hull*

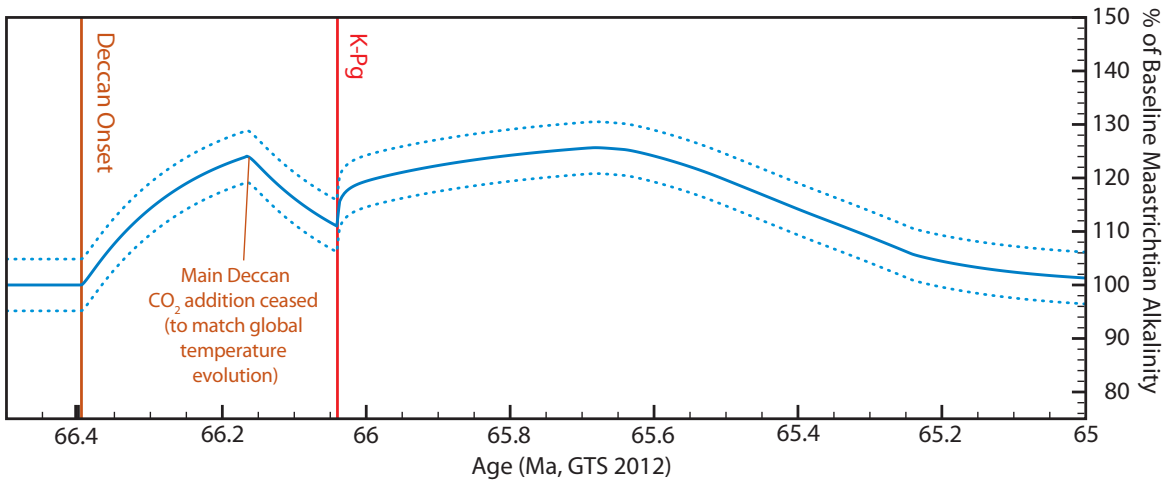

Fig. S13. Evolution of Total Alkalinity assumed over the K-Pg. The solid line represents the relative change in alkalinity in an ocean basin- in this example the surface Atlantic box - over the events of the K-Pg. This simulation from (22) attempts to fit the evolution of temperature during magnetochron C29r (through maximum CO_2 outgassing early in C29r, and a small fraction after the boundary), as well as the evolution of the CCD after the K-Pg boundary (through a 50% reduction in the $CaCO_3$:C_{org} ratio for the first 200 kyr, tapering back to pre-event values over 200 kyr). The dotted lines on either side of the solid line represent the ± 100 μmol kg^{-1} uncertainty applied to alkalinity estimates during uncertainty propagation (see Section D).

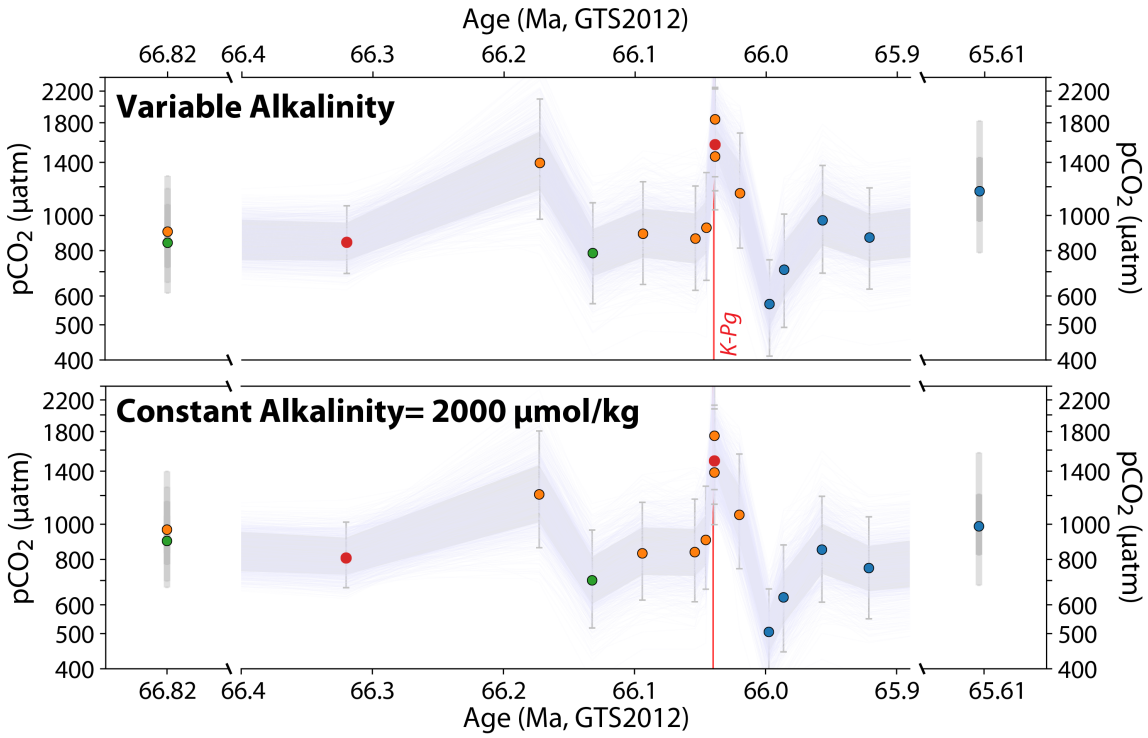

Fig. S14. Evolving Alkalinity vs. Invariant alkalinity. Our preferred solution (top panel) is compared to a scenario with the same $\delta^{11}B_{sw}$ but a constant value of alkalinity of 2000 μmol kg^{-1} for all data-points. The main features of the record remain, despite minor differences. As in main text Figure 1, the shaded grey area denotes 1σ uncertainty, with the error bars denoting 2σ (each purple line plotted is one of 1,000 Monte Carlo simulations).

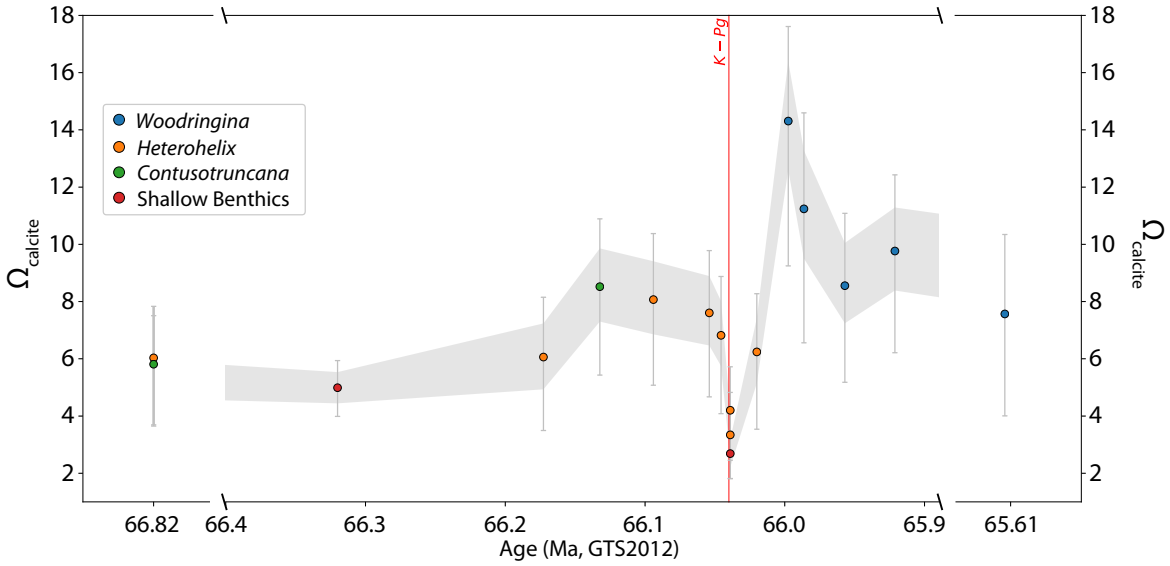

Fig. S15. Extreme oversaturation after the K-Pg. Ω_{calcite} at a $\delta^{11}B_{sw}$ of 39.45 $\pm$ 0.4 ‰ and evolving alkalinity over the K-Pg from Fig. S13. The shaded grey area denote 68% quantiles of our Monte Carlo simulations, and error bars are 95 % quantiles.

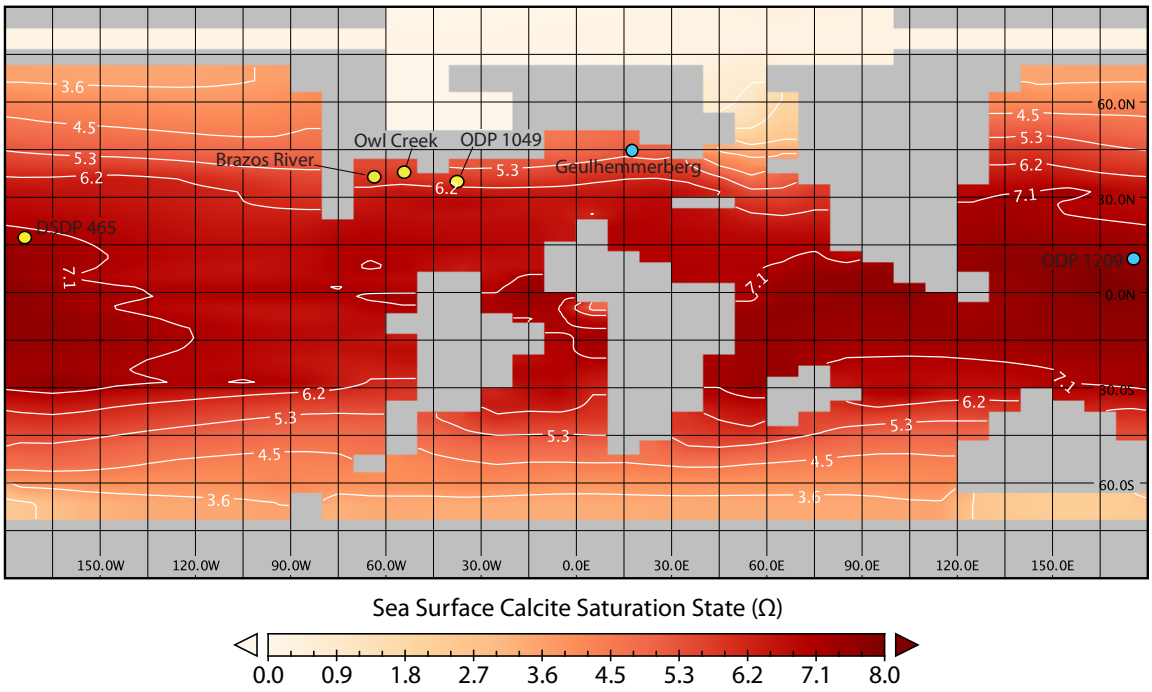

Fig. S16. Sea-surface Calcite Saturation in our control Maastrichtian simulation. Sites marked with yellow circles are those where we have measured δ^{11}B during the Maastrichtian. For these samples, we use the constraint that their Ω_{Calcite} should have fallen between 5 and 7.5 to constrain $\delta^{11}B_{sw}$.

Michael J. Henehan*, Andy Ridgwell, Ellen Thomas, Shuang Zhang, Laia Alegret, Daniela N. Schmidt, James W. B. Rae, James D. Witts, Neil H. Landman, Sarah E. Greene, Brian T. Huber, James Super, Noah J. Planavsky and Pincelli M. Hull*

$\delta^{11}B_{sw}$ (‰)	Samples w/median simulated $\Omega > 10$	Samples w/median $\Omega > 15$	Samples with $\Omega >$ 10 at $>$ 95% conf.	Samples w/median Simulated $\Omega < 1$	Samples w/$\Omega < 1$ at $>$ 95% conf.	Feasible AOU?	Median Maast. C30n $\Omega_{Surface}$ outside 5 - 7.5	Maas. C30n $\Omega_{Surface}$ outside 5 - 7.5 at 95% conf.	Median Maastrichtian (incl. C29r) $\Omega_{Surface}$ outside 5 - 7.5	Maastrichtian (incl. C29r) $\Omega_{Surface}$ outside 5 - 7.5 at 95% conf.
38.45	7	1	3	0	0	Y	2	0	7	3
38.5	7	1	3	0	0	Y	2	0	7	3
38.55	7	1	2	0	0	Y	2	0	7	3
38.6	6	1	2	0	0	Y	2	0	7	3
38.65	5	1	2	0	0	Y	1	0	6	3
38.7	5	1	2	0	0	Y	1	0	6	3
38.75	5	1	1	0	0	Y	0	0	5	2
38.8	4	1	1	0	0	Y	0	0	5	2
38.85	3	1	1	0	0	Y	0	0	5	2
38.9	3	1	1	0	0	Y	0	0	5	1
38.95	3	1	1	0	0	Y	0	0	4	1
39	3	0	1	0	0	Y	0	0	4	1
39.05	3	0	1	0	0	Y	0	0	4	0
39.1	3	0	1	0	0	Y	0	0	4	0
39.15	3	0	1	0	0	Y	0	0	3	0
39.2	3	0	1	0	0	Y	0	0	3	0
39.25	3	0	1	0	0	Y	0	0	3	0
39.3	2	0	1	0	0	Y	0	0	4	0
39.35	2	0	1	0	0	Y	0	0	3	0
39.4	2	0	1	0	0	Y	0	0	3	0
39.45	2	0	1	0	0	Y	0	0	4	0
39.5	2	0	1	0	0	Y	0	0	3	0
39.55	2	0	1	0	0	Y	0	0	3	0
39.6	2	0	1	0	0	Y	0	0	3	0
39.65	2	0	1	0	0	Y	0	0	3	0
39.7	2	0	1	0	0	Y	0	0	3	0
39.75	2	0	1	0	0	Y	0	0	3	0
39.8	2	0	1	0	0	Y	0	0	2	0
39.85	2	0	1	0	0	Y	0	0	2	0
39.9	2	0	0	1	0	N	0	0	2	1
39.95	2	0	0	1	0	N	0	0	3	1
40	2	0	0	2	0	N	0	0	3	1
40.05	2	0	0	2	1	N	0	0	3	1
40.1	2	0	0	2	1	N	1	0	4	1

Table S2. Evaluation of the feasibility of different $\delta^{11}B_{sw}$ scenarios for the Cretaceous-Palaeogene. Description of each of the criteria is given in the text. Beyond 40.1, >5% of simulations are mathematically unresolvable, leading to increasingly spurious distributions of other carbonate system parameters as $\delta^{11}B_{sw}$ increases (for example, at 40.6 ‰, >75% of simulations for some samples are mathematically unresolvable). Dotted lines demark the range of plausible $\delta^{11}B_{sw}$ over the K-Pg.

D. Uncertainty Propagation. Because of the complexities of these calculations, and the many sources of uncertainty to be incorporated, we utilise Monte Carlo simulations to incorporate our sources of uncertainty (outlined below).

- Uncertainty on **boron isotope measurements** (see Section A) at the 2σ level.
- Uncertainty of 3% (2σ) on initial **Mg/Ca measurements** (see Section A), which is propagated through boron isotope-pH calculations, O_2 solubility, K constant and carbonate system calculations.
- Uncertainty on model-derived estimates of **total alkalinity**, and the evolution of alkalinity through time (see Section B), are hard to quantify, but we assign an uncertainty of ± 100 μmol kg^{-1}. Note that the Alkalinity assigned does not have a sizeable impact on our findings; see Fig. S14
- Values for **salinity** are taken from our Maastrichtian control GENIE simulation (see Section A). Uncertainty in each assigned salinity value was set at ± 1 psu, which in turn was propagated into the calculation of Ionic Strength for K constant calculations (via the relationship between salinity and Ionic strength (Eq. 5) from ref. (142)), and the calculation of total [B] (Eq. 6; note with constant 380 lower than 432.6 today, because of the lower [B] in Cretaceous seawater- see section A). Note however that salinity does not introduce substantial uncertainty on boron and carbonate system calculations (e.g. (87)).

$$I = \frac{(19.924 * \text{Salinity})}{1000 - (1.005 * \text{Salinity})} \quad [5]$$

$$[\text{B}]_{\text{total}} = 380 * \frac{\text{Salinity}}{35} \quad [6]$$

- Uncertainty in the **vital effect correction** between epifaunal benthics and *Heterohelix globulosa* (see Section 3) is accounted for, since for each Monte Carlo replicate dataset (with different $\delta^{11}B_{CaCO_3}$ and pK_B^*) produces a different offset in microenvironment pH between these foraminifera, which is then applied to other samples in that replicate dataset where necessary, and propagated through several iterations of pH and pH-corrected temperature calculations.
- Finally, for our final pH and pCO_2 calculations, $\delta^{11}B_{sw}$ is allowed to vary between 39.05 and 39.85 (see Section C and TableS2).

Once all calculations are complete, the median value of the Monte Carlo distributions of any given parameter are taken as our estimate of the 'true' value. 1 and 2 σ confidence intervals are calculated as the 16 - 84 % and 2.5 - 97.5% quantiles of the array of simulations respectively. At high $\delta^{11}B_{sw}$ some Monte Carlo replicate datasets become mathematically unresolvable (i.e. simulated sample datasets have δ^{11}B values lower than borate could possibly be at that $\delta^{11}B_{sw}$, even accounting for microenvironment alteration), and so we monitor the number of simulations that fail. Since these 'failures' will always be on the low-pH tail of the distribution, and the calculable members of the array will always be those on the high-pH tail of the array, resultant statistics will be subject to a bias. For this reason, we do not present data from $\delta^{11}B_{sw}$ iterations where >5% of simulations failed (see TableS2).

6. GENIE Simulations

A. Boundary Conditions. We employ the cGENIE Earth system model of intermediate complexity, which consists of a three-dimensional ocean circulation model and a two-dimensional atmosphere energy-moisture-balance model with sea-ice, coupled to a marine carbon cycle based around a single limiting nutrient (PO_4^{3-}) (143) and a surface ocean particulate organic matter (POM) export scheme that follows ref.(144). For this study, cGENIE was configured with a Maastrichtian bathymetry and continental configuration (Fig. S17), which is based on the paleogeography of ref.(41), but with lower resolution for practicality of computing. This loss of resolution means that some small features of Markwick and Valdes' paleogeography are lost, including a narrow, shallow (< 50 m; (145)) Arctic-North Atlantic connection between Greenland and Norway. Although in other time periods these connections can be critical in determining global thermohaline circulation patterns (e.g. (146, 147)), in the Maastrichtian, modelling has demonstrated that these gateways have limited influence (145, 148, I. Niezgodzki, pers. comm., 2019). In addition, bulk and foraminiferal carbonates from the K-Pg North Atlantic record δ^{18}O values that are not indicative of significant input of low-salinity Arctic water into this region (149–151, this study), supporting our model configuration as being representative. We apply an annual average wind-stress field transformed to a 36×36 equal-area grid and a zonal planetary albedo distribution from ref. (152). The solar constant is reduced by 0.56 % appropriate for the Late Cretaceous. The ocean is initialised with global average concentrations of Ca^{2+} and Mg^{2+} of 19.1 and 29.1 mmol kg^{-1}, respectively (153), and 10.0 mmol kg^{-1} SO_4^{2-} (range: 6-14 mmol kg^{-1})(154). Nutrient (PO_4^{3-}) concentrations are set at modern (143), and a uniform $CaCO_3$:Particulate Organic Carbon (POC) export ratio of 0.2 was assumed (155). Ocean salinity is decreased by 1 PSU to reflect the likely absence of significant land-based ice.

In our preferred scenario radiative forcing is initially set at 850 ppm CO_2, with global weathering fluxes of 20 Tmol yr^{-1} Ca^{2+} split evenly between carbonate and silicate weathering. This weathering influx is similar to those suggested for the Maastrichtian (156), but the sensitivity of our experimental findings to this assumption was tested (see Section B below). Resulting model climatology in our preferred run is characterised by a mean global sea surface temperature (SST) of 26.6 °C (compared to 19.2 °C for a pre-industrial configuration), and average benthic (>2000 m water depth) temperatures of around 9.5 °C - close to δ^{18}O-derived estimates for this time (34, 54). Resultant mean global alkalinity (ALK) is 1987 μmol kg^{-1}, giving a mean surface concentration (∼1927 μmol kg^{-1}) close to previous reconstructions of Late Cretaceous seawater (131, 153). This Maastrichtian cGENIE configuration predicts a source of North Pacific intermediate-to-deep water overlying denser water from the South, consistent with Neodymium isotopic inferences for the late Mesozoic and early Cenozoic (e.g., refs (43, 157)). By adjusting initial atmospheric $\delta^{13}C_{CO_2}$ to -4.5 ‰, we could reproduce late Maastrichtian vertical δ^{13}C gradients in the

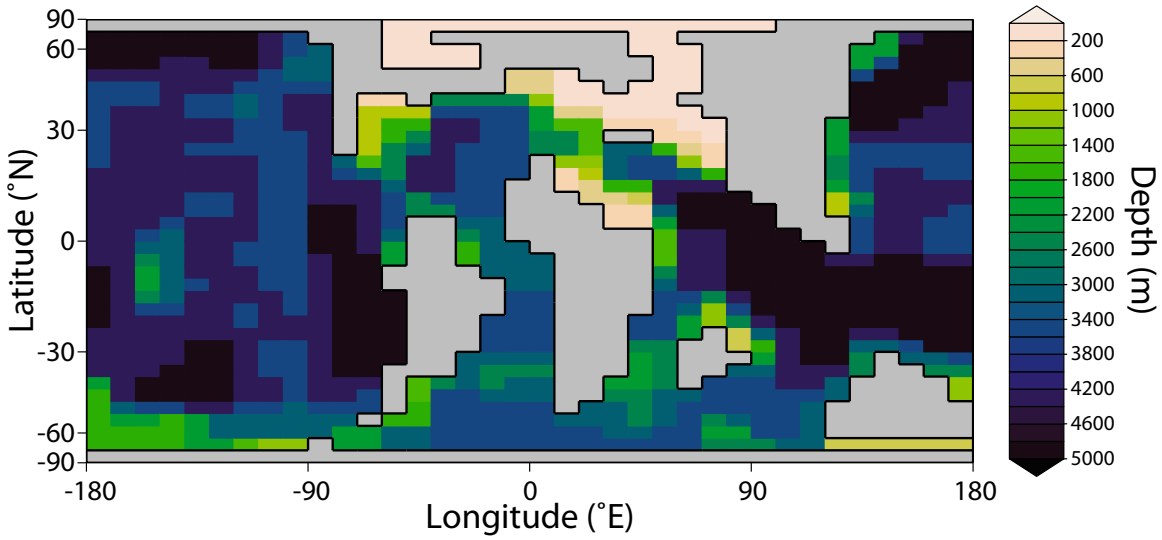

Fig. S17. Continental configuration boundary conditions used for K-Pg Genie simulations.

Pacific successfully (see Fig. S18), and achieve an approximate match between observed surface open-ocean Pacific (bulk $CaCO_3$) $\delta^{13}C$ and model-predicted (surface) $\delta^{13}C_{DIC}$ (Table S3).

For all K-Pg carbon cycle experiments, cGENIE was first spun up to equilibrium at a given pCO_2 and a given global weathering flux (see Section B below), by holding pCO_2 constant and allowing carbonate sedimentation patterns and ocean saturation to adjust to chosen weathering fluxes through fully open, dynamic carbonate burial and compensation processes. Once stabilised at a given pCO_2 and steady-state TAlk and DIC, this simulation was used as a starting point for subsequent experimental manipulations of marine carbon cycling. These manipulations were carried out in a closed configuration, with $CaCO_3$ production and export from the surface ocean, but no tracers gained via riverine inputs or lost through sedimentation (note, ocean-atmosphere gaseous exchange is permitted).

B. Experimental Design. To examine the manifestation of different marine carbon cycling changes in vertical $\delta^{13}C$ and pH gradients, we carried out an ensemble of cGENIE runs changing either a) the depth of organic matter remineralisation (to test the 'Living Ocean'-type scenario) or b) reductions in new primary production (to test 'Strangelove'-type scenarios). Specifically, organic matter remineralisation depth was altered by changing the 'e-folding' depth; that is, the depth in the water column at which $\sim$37 %, (or $1/e$) of the organic carbon originally produced at the surface survives (159). Following ref.(160) our control scenario has a modern e-folding depth of $\sim$589 m. We test two scenarios of shallowed remineralisation (one more extreme e-folding depth of 60m and one more moderate 200m), and a greater-than-modern depth of remineralisation (1000 m) for comparison. To simulate a reduction in new primary production in GENIE we adjust biological export production by re-scaling the net removal (organic matter transformation) rate for a given $[PO_4^{3-}]$ at the surface (K_{PO_4} (143)), so as to mimic a post-extinction ocean that was relatively depleted in primary producers. Specifically, we reduce biological PO_4^{3-} uptake to 50 %, 40 %, 30 %, 18 %, 13 %, 9 %, 6 %, 3 % and 0 % of default control values, which translate to a reduction of global POC export to 84 %, 77 %, 68 %, 50 %, 40 %, 30 %, 20 %, 10 % and 0 % of the control scenario (6.23 Pg C yr^{-1}) respectively. This non-linear relationship between changes in organic matter transformation and POC export is caused by a buildup in under-utilised $[PO_4^{3-}]$ in the surface ocean, which partially compensates for a loss of $[PO_4^{3-}]$ transformation efficiency. Simulated $\delta^{13}C$ and pH profiles at Shatsky Rise (then Central Pacific) in each case are plotted in Fig. S19. Further details of the various experiments are given in Table S3. All experiments manipulating the biological pump were run for 10,000 years, starting from a Maastrichtian equilibrium spin-up at the chosen pCO_2 and global weathering input.

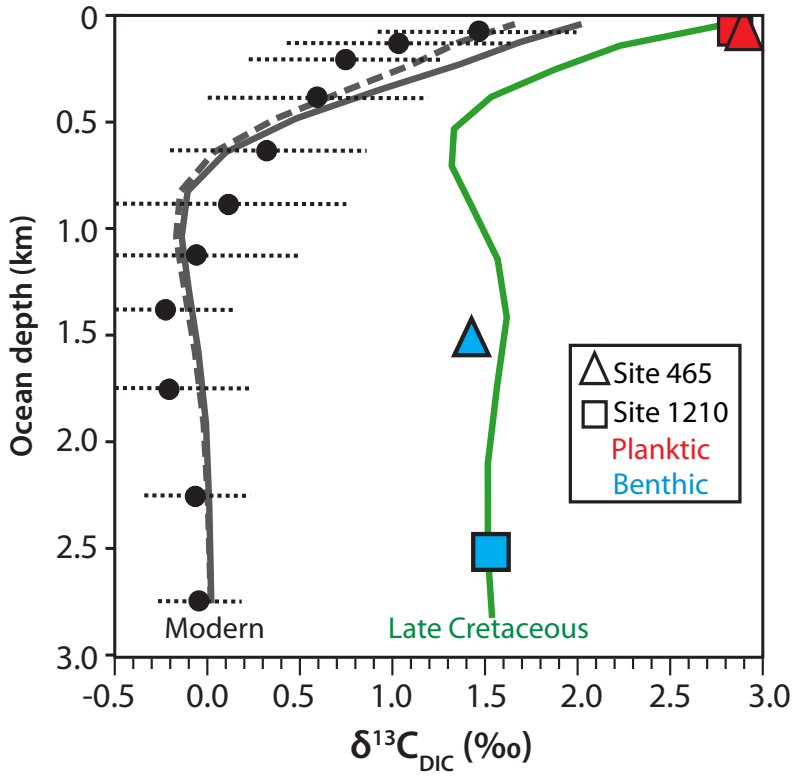

Fig. S18. Observed and modelled Pacific vertical ocean δ^{13}C gradients. Modern (pre-Industrial) Pacific basin-averaged depth profiles in δ^{13}C predicted by GENIE are shown as a solid grey line. Basin-averaged observations (158) are shown as filled circles with error estimates. The apparent model overestimate at the surface is due to the historical decrease in atmospheric δ^{13}C due to fossil fuel emissions. Taking this into account in the model (dashed grey line) improves the fit to the data assuming model year 1976 is representative of the GEOSECS data. On the right side, observed values of carbonate δ^{13}C are compared to the δ^{13}C profile from our control late Maastrichtian cGENIE scenario at the approximate location of Shatsky Rise (K_{ctrl}; dark green line). The observed pre-impact surface (red) and benthic (blue) $CaCO_3$ δ^{13}C values are shown for Pacific Ocean Sites 1210 (squares; 2000-3000 m estimated palaeodepth) and 465 (triangles; ∼1500 m). These values are averages over 50 kyr calculated from ref. (11).

Michael J. Henehan*, Andy Ridgwell, Ellen Thomas, Shuang Zhang, Laia Alegret, Daniela N. Schmidt, James W. B. Rae, James D. Witts, Neil H. Landman, Sarah E. Greene, Brian T. Huber, James Super, Noah J. Planavsky and Pincelli M. Hull*

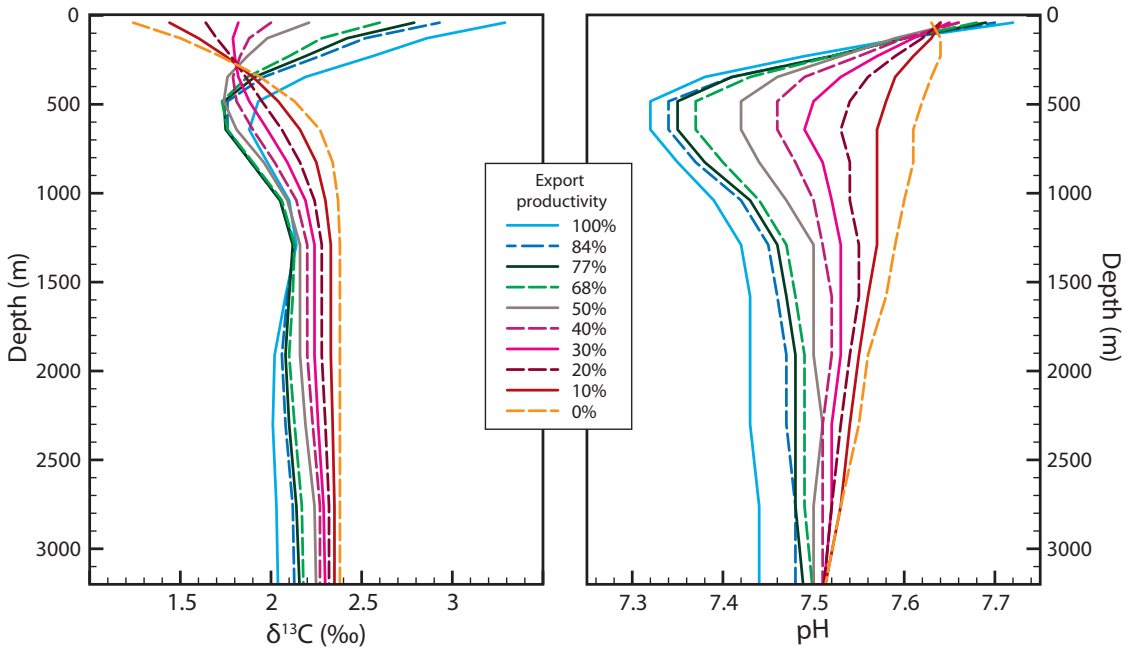

Fig. S19. Carbon isotope and pH profiles at Shatsky Rise. Shown are the simulations for a starting pCO_2 of 850 ppm and a weathering input of 20 Tmol yr^{1}. For the effect of these baseline conditions on our experiments see Figs. S21 and S22.

Model run ID	POC export[1] (PgC yr^{-1})	$CaCO_3$ export (PgC yr^{-1})	Atmospheric pCO_2 (ppm)	Atmospheric $\delta^{13}C_{DIC}$ (‰)	Surface $\delta^{13}C_{DIC}$[2] (‰)	Benthic $\delta^{13}C_{DIC}$[3] (‰)	$\Delta pH_{surf\text{-}deep}$	Notes
$K_{control}$	6.23	1.25	869	-4.67	2.78	1.53	0.283	Maastrichtian Control Run[4]
					2.84	1.53		**Late Maastrichtian[5]: ODP Site 1210**(11)
1000m e-folding depth	5.02 (81%)	1.00	735	-4.52	3.03	1.30	0.489	
200m e-folding depth	9.58 (154%)	1.92	1115	-4.89	2.39	1.74	0.004	'Living Ocean' Scenario, $\Delta pH \sim 0$
60m e-folding depth	12.96 (208%)	2.59	1253	-4.91	2.24	1.73	-0.123	
50 % Export Productivity	3.1	0.62	1047	-5.59	1.71	1.72	0.158	$\Delta\delta^{13}C_{DIC} \sim 0‰$
40 % Export Productivity	2.45	0.49	1075	-5.76	1.5	1.75	0.143	
30 % Export Productivity	1.87	0.37	1100	-5.9	1.32	1.78	0.131	
21 % Export Productivity	1.3	0.26	1123	-6.05	1.14	1.81	0.119	
11 % Export Productivity	0.68	0.14	1149	-6.21	0.94	1.84	0.106	
0 % Export Productivity	0 (0%)	0	1176	-6.37	0.74	1.88	0.093	'Strangelove Ocean' Scenario
					1.77	1.73		**Post-Event[6]: ODP Site 1210**(11)

Table S3. Summary of GENIE Model runs at 850 ppm pCO_2 and 20 T mol yr^{-1} weathering input. ΔpH is pH at 0-80 m depth at Shatsky Rise minus the pH at 2500 m. [1] POC export from the surface ocean. Biological export production is adjusted in GENIE by re-scaling the net removal (organic matter transformation) rate for a given [PO_4^{3-}] at the surface (K_{PO_4} (143)). This means that a build-up of PO_4^{3-} in the surface ocean will act to partially counteract the effect of the imposed change. In the changing remineralisation depth scenarios, shallower remineralisation results in more nutrients being retained at shallower depths, hence POC export from the surface in these cases appears higher. [2]Model 'surface' (average 0-80 m water depth) $\delta^{13}C_{DIC}$ at Shatsky Rise. [3]Model benthic ($\sim$2500 m water depth) at Shatsky Rise. [4]Control run, with e-folding depth set to 589 m, and PO_4^{3-} uptake at full capacity. [5]Observed pre-event $\delta^{13}C$ values are averaged over 50 kyr. [6]Observed post-event $\delta^{13}C$ values are averaged over 200 kyr, excluding the first 10 kyr.

In these runs, climate can evolve in response to predicted changes in atmospheric CO_2, but the ocean TAlk inventory and ocean+atmospheric CO_2 in these 'closed-system' runs do not change. This is in part because the model does not appropriately represent organic carbon burial (and associated nutrient removal), and in part because exploring the full range of possible changes in chemical weathering fluxes, PIC:POC export ratios, respiration-driven pore-water carbonate dissolution, and major ion chemistry over the K-Pg boundary is beyond the scope of this study. To address how much our biogeochemical perturbation experiments are influenced by changes in ambient TAlk, [DIC] or pCO_2, however, we ran the same experiments across a range of starting pCO_2 (600, 850 and 1200 ppm) and global weathering régimes (10, 15 and 20 Tmol yr^{-1}) to produce a range of steady state TAlk and [DIC] (Fig. S20).

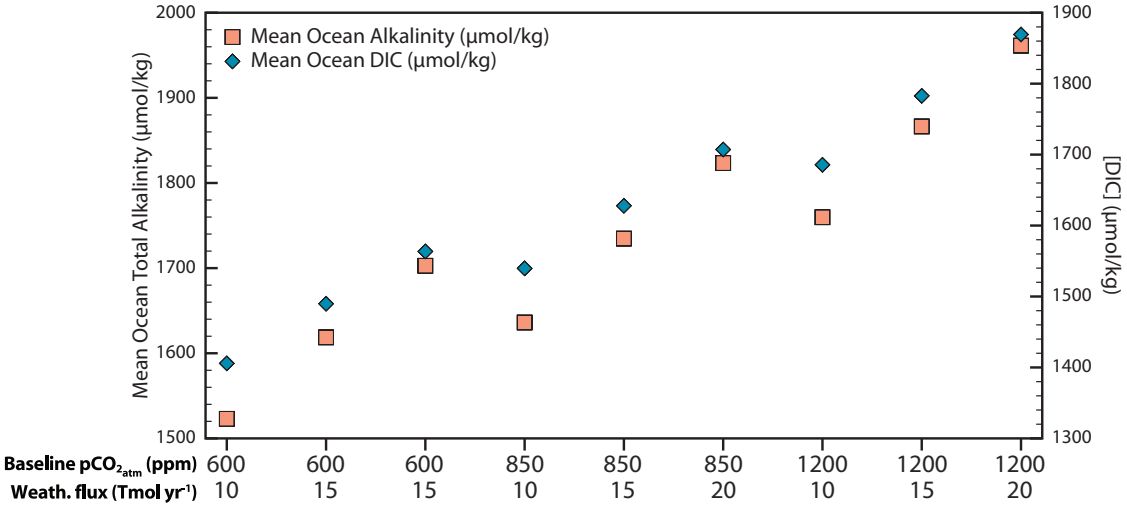

Fig. S20. Baseline alkalinity and [DIC] states tested. Shown are the mean surface ocean Total Alkalinity and mean surface ocean [DIC] for each model parameter set. For the effect of these baseline conditions on our experiments see Figs. S21 and S22.

The starting pCO_2 and ocean chemistry have some influence on vertical $\delta^{13}C$ (Fig. S21) and pH (Fig. S22) gradients. Higher TAlk implies greater concentration of surface-ocean DIC in equilibrium for a given atmospheric pCO_2, and hence slightly smaller late Maastrichtian $\Delta\delta^{13}C$. Conversely, reducing TAlk reduces DIC and hence increases the relative importance of respired POC in lowering $\delta^{13}C$ at depth. Despite these differences, our conclusions are essentially unchanged across mean ocean alkalinity ranging from 1523 to 1961 μmol kg^{-1}. While a period of extreme carbonate over-saturation after the K-Pg (e.g. refs. (22, 31), this study) would have made it easier to dampen pH and $\delta^{13}C$ gradients for any given change in remineralisation/production, the magnitude of change is unlikely to be large enough to produce the observed patterns in $\delta^{11}B/\delta^{13}C$.

Reducing primary productivity to nil in our 'Strangelove' scenario flattens, or indeed reverses, carbon isotope gradients between the surface and deep ocean as expected (Fig. S21, Fig. 2, main text). However, our model simulations also demonstrate that such a reduction in carbon isotope gradient can also be attained with productivity reduced to ~50% of its Maastrichtian state. This is due to the contribution from the the solubility pump to ocean $\delta^{13}C$ distributions. The fractionation between dissolved $CO_{2(aq)}$ (and thus atmospheric pCO_2) and aqueous bicarbonate (and thus dissolved inorganic carbon, DIC) increases by about 0.1 ‰ per °C cooling, such that the surface $\delta^{13}C_{DIC}$ at colder, higher latitudes will tend to be driven higher with respect to the atmosphere compared to the warmer, low-latitude ocean surface. Colder high-latitude waters ventilate the deep ocean, so the solubility pump imparts an 'inverted' planktic-benthic gradient throughout low and mid latitudes, with $\delta^{13}C$ higher at depth and lower at the surface. The effect of the solubility pump on marine $\delta^{13}C_{DIC}$ is shown in Fig. 3, main text. Typically, the action of the biological pump, in which isotopically depleted organic matter is removed from the surface and remineralised at depth, overprints this pattern to give the observed 'normal' sign of $\Delta\delta^{13}C$, with most positive values at the surface. At the K-Pg, however, this underlying process meant that the biological pump needed only to be partially weakened to be overwhelmed by the isotopic effect of the solubility pump, and hence collapse the surface-to-deep $\delta^{13}C$ gradient. Thus the underlying action of the solubility pump helps to reconcile the long-standing paradox of collapsed carbon isotope gradients without extinction in deep-sea benthic foraminifera at the K-Pg boundary, despite benthic foraminifera relying on export of organic matter from the surface ocean for their food supply.

Finally, our simulations also help to explain the spatially-varied patterns of productivity change that have been reported across the K-Pg, as summarised in ref. (26). These observations of a 'Heterogenous Ocean' are often linked to the idea that some regions may have been more or less affected by the K-Pg mass extinction (e.g. (161)). In fact, heterogenous patterns of export productivity change are to be expected from an ocean still recovering from extinction. Under typical late-Cretaceous conditions, with a pelagic ecosystem that is fully adapted to exploit available nutrient stocks to their maximum extent, there were likely, as today, large swathes of highly oligotrophic waters, where export productivity was low (Fig. S23a). As mass extinction meant that pelagic ecosystems were no longer as efficient at utilising available nutrients, on a global scale, export productivity decreased (e.g Fig. S23b). However, the reservoir of nutrients in the surface ocean would have risen as a result of this incomplete exploitation, and as a result, locations that were previously starved of nutrients could have experienced stable, or even increased, nutrient availability and export productivity even while on a global scale productivity was reduced.

In Fig. S24, we plot POC export from the surface ocean in our 50% export productivity scenario (which successfully reproduced flat $\delta^{13}C$ gradients) relative to the K-Pg control scenario. As is clear, in many regions that were previously oligotrophic (Fig. S23), productivity was

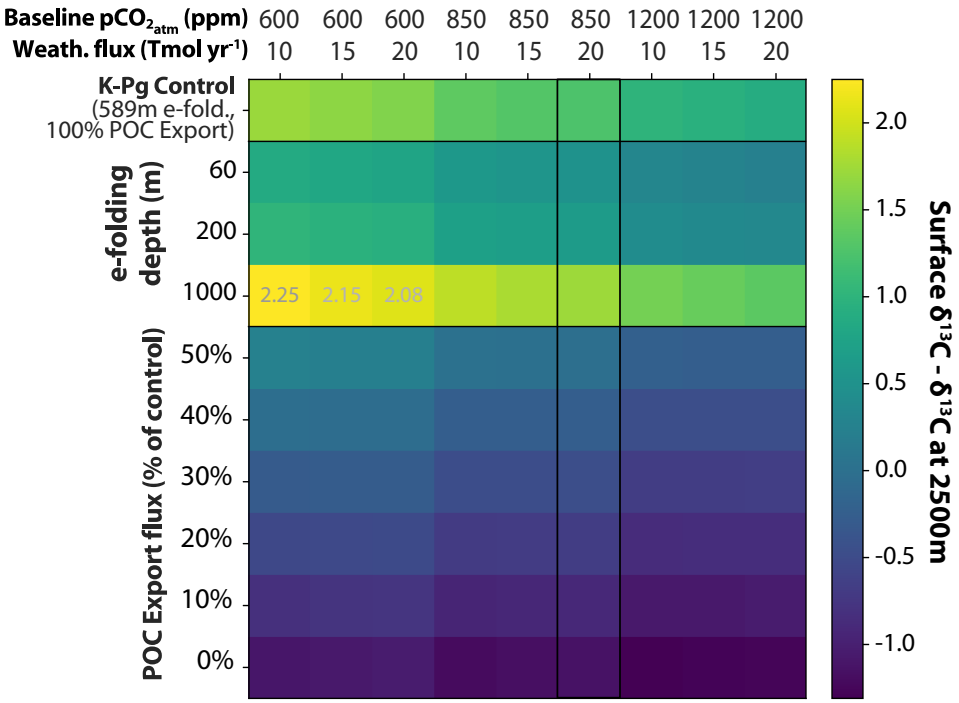

Fig. S21. The influence of baseline pCO_2 and ocean chemistry conditions on vertical $\delta^{13}C_{DIC}$ gradients. Shown are modelled surface minus benthic $\delta^{13}C_{DIC}$ values for each chosen parameter set. Our preferred scenario (850 ppm pCO_2, 20 Tmol yr^{-1} weathering influx) is outlined in black. Minor differences in $\delta^{13}C$ gradient are stem from starting conditions, but the conclusion that muted $\delta^{13}C$ gradients can be produced by shallow organic matter remineralisation and or changes in new primary production remains essentially unchanged across mean ocean alkalinity ranging from 1523 to 1961 μmol kg^{-1}.

maintained at or above pre-impact levels despite globally-reduced productivity. Our Pacific sites, given the uncertainty of palaeogeographic reconstruction and modelling, could well have fallen within a zone of maintained or elevated productivity, thereby reconciling the globally-lowered productivity suggested by vertical $\delta^{13}C$ and $\delta^{11}B$ gradients with productivity indicators from this region (11, 26). Indeed patterns of regional productivity change predicted by our 50% productivity scenarios agree with proxy records from other basins (26), suggesting that the 'Heterogenous Ocean' is an expected feature of a world with globally reduced productivity, rather than necessarily any signal of e.g. differential severity of the effects of impact.

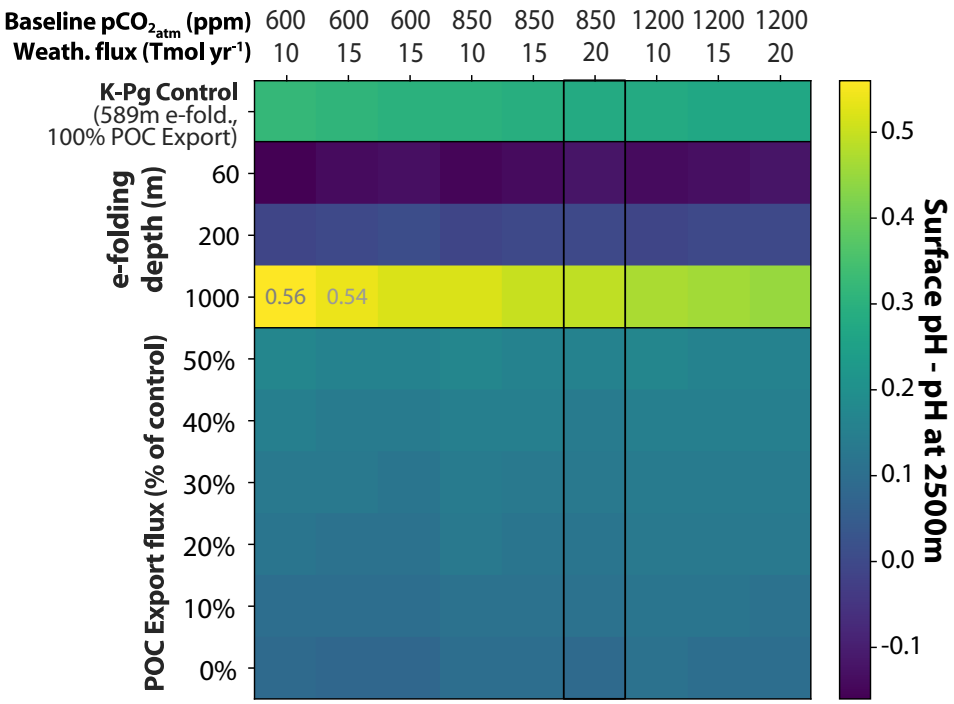

Fig. S22. The influence of baseline pCO_2 and ocean chemistry conditions on vertical pH gradients. Shown are the surface minus benthic pH values at Shatsky Rise. Our preferred scenario (850 ppm CO_2, 20 Tmol yr^{-1} weathering influx) is outlined in black. While clearly changes in remineralisation depth and POC production and export have a strong influence on vertical pH gradients, the effect of starting pCO_2 and ocean chemistry is rather more muted. Therefore our main conclusion, that shallowing of the depth of remineralisation is key to attaining flattened vertical pH gradients, stands regardless of boundary conditions.

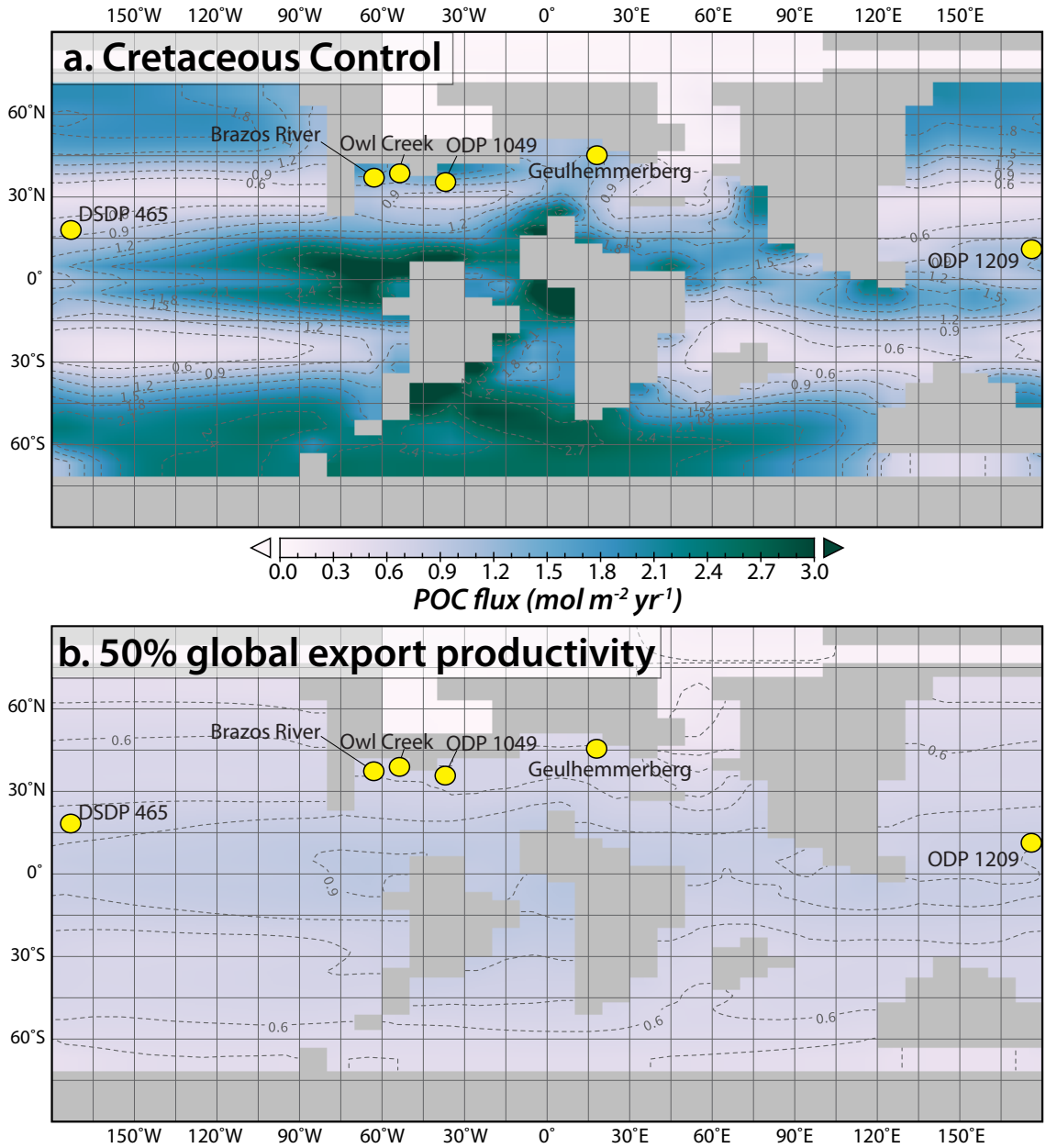

Fig. S23. Geographic patterns in Export Productivity predicted by GENIE. Geographic patterns of export productivity from the surface ocean in our Control Cretaceous scenario (panel a) and our 50% loss of export productivity scenario (panel b). Approximate palaeolocations of sample sites are shown in yellow.

Michael J. Henehan*, Andy Ridgwell, Ellen Thomas, Shuang Zhang, Laia Alegret, Daniela N. Schmidt, James W. B. Rae, James D. Witts, Neil H. Landman, Sarah E. Greene, Brian T. Huber, James Super, Noah J. Planavsky and Pincelli M. Hull*

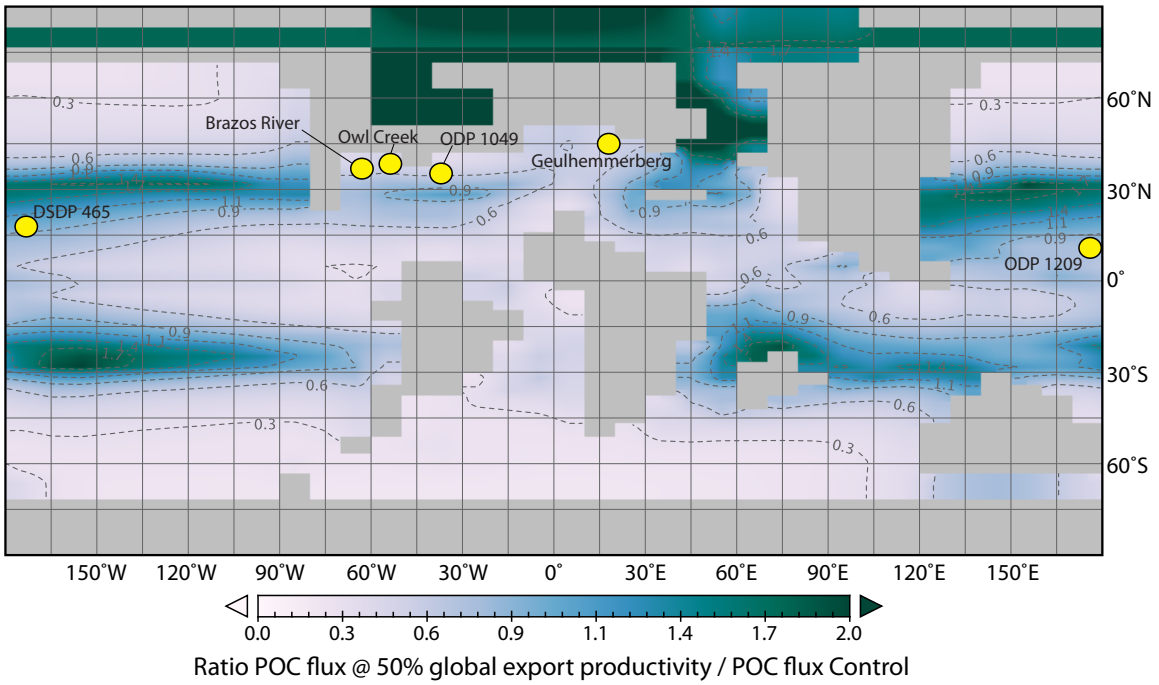

Fig. S24. Geographic patterns of relative productivity change. Because nutrient buildup in the surface ocean acts to counteract inefficiency in nutrient exploitation in depauperate post-extinction pelagic ecosystems, more nutrients reached regions of the surface ocean that were previously oligotrophic. As a result, their relative productivity could have increased even when the global average productivity was significantly reduced.

References

1. Schulte P, et al. (2010) The Chicxulub Asteroid Impact and Mass Extinction at the Cretaceous-Paleogene Boundary. *Science* 327(5970):1214–1218.
2. Kring DA (2007) The Chicxulub impact event and its environmental consequences at the Cretaceous-Tertiary boundary. *Palaeogeography, Palaeoclimatology, Palaeoecology* 255(1-2):4–21.
3. Brugger J, Feulner G, Petri S (2017) Baby it's cold outside: Climate model simulations of the effects of the asteroid impact at the end of the Cretaceous. *Geophysical Research Letters* 44(1):419–427.
4. Sprain CJ, et al. (2019) The eruptive tempo of Deccan volcanism in relation to the Cretaceous-Paleogene boundary. *Science* 363(6429):866–870.
5. Schoene B, et al. (2019) U-Pb constraints on pulsed eruption of the Deccan Traps across the end-Cretaceous mass extinction. *Science* 363(6429):862–866.
6. Smit J, Brinkhuis H (1996) The Geulhemmerberg Cretaceous/Tertiary boundary section (Maastrichtian type area, SE Netherlands); summary of results and a scenario of events. *Geologie en Mijnbouw* 75:283–293.
7. Larina E, et al. (2016) Upper Maastrichtian ammonite biostratigraphy of the Gulf Coastal Plain (Mississippi Embayment, southern USA). *Cretaceous Research* 60:128–151.
8. Leighton AD, Hart MB, Smart CW, Leng MJ, Hampton M (2017) Timing recovery after the Cretaceous/Paleogene Boundary: Evidence from the Brazos River, Texas, USA. *Journal of Foraminiferal Research* 47(3):229–238.
9. Dutkiewicz S, et al. (2015) Impact of ocean acidification on the structure of future phytoplankton communities. *Nature Climate Change*.
10. Prinn RG, Fegley Jr. B (1987) Bolide impacts, acid rain, and biospheric traumas at the Cretaceous-Tertiary boundary. *Earth and Planetary Science Letters* 83(1-4):1–15.
11. Alegret L, Thomas E, Lohmann KC (2012) End-Cretaceous marine mass extinction not caused by productivity collapse. *Proceedings of the National Academy of Sciences* 109(3):728–732.
12. D'Hondt S, Pilson MEQ, Sigurdsson H, Hanson AK, Carey S (1994) Surface-water acidification and extinction at the Cretaceous-Tertiary boundary. *Geology* 22(11):983–986.
13. Hart MB, Leighton AD, Hampton M, Smart CW (2019) Global bioevents and the Cretaceous/Paleogene boundary in Texas and Alabama: Stratigraphy, correlation and ocean acidification. *Global and Planetary Change* pp. S0921–8181(18)30079–1.
14. Bowman VC, Francis JE, Riding JB, Hunter SJ, Haywood AM (2012) A latest Cretaceous to earliest Paleogene dinoflagellate cyst zonation from Antarctica, and implications for phytoprovincialism in the high southern latitudes. *Review of Palaeobotany and Palynology* 171:40–56.
15. Hollis CJ (1993) Latest Cretaceous to Late Paleocene radiolarian biostratigraphy: A new zonation from the New Zealand region. *Marine Micropaleontology* 21(4):295–327.
16. Liu YW, Eagle RA, Aciego SM, Gilmore RE, Ries JB (2018) A coastal coccolithophore maintains pH homeostasis and switches carbon sources in response to ocean acidification. *Nature Communications* 9(1):2857.
17. Henehan MJ, et al. (2017) Size-dependent response of foraminiferal calcification to seawater carbonate chemistry. *Biogeosciences* 14(13):3287–3308.
18. Bown P (2005) Selective calcareous nannoplankton survivorship at the Cretaceous-Tertiary boundary. *Geology* 33(8):653–656.
19. D'Hondt SL, Keller G (1991) Some patterns of planktic foraminiferal assemblage turnover at the Cretaceous-Tertiary boundary. *Marine Micropaleontology* 17(1-2):77–118.
20. Ohno S, et al. (2014) Production of sulphate-rich vapour during the Chicxulub impact and implications for ocean acidification. *Nature Geoscience* 7(4):279–282.
21. Tyrrell T, Merico A, Armstrong McKay DI (2015) Severity of ocean acidification following the end-Cretaceous asteroid impact. *Proceedings of the National Academy of Sciences* p. 201418604.
22. Henehan MJ, Hull PM, Penman DE, Rae JWB, Schmidt DN (2016) Biogeochemical significance of pelagic ecosystem function: an end-Cretaceous case study. *Phil. Trans. R. Soc. B* 371(1694):20150510.
23. Hsu KJ, et al. (1982) Mass Mortality and Its Environmental and Evolutionary Consequences. *Science* 216(4543):249–256.
24. Hsü KJ, McKenzie JA (1985) A "Strangelove" ocean in the earliest Tertiary in *Geophysical Monograph Series*, eds. Sundquist ET, Broecker WS. (American Geophysical Union, Washington, D. C.) Vol. 32, pp. 487–492.
25. D'Hondt S, Donaghay P, Zachos JC, Luttenberg D, Lindinger M (1998) Organic Carbon Fluxes and Ecological Recovery from the Cretaceous-Tertiary Mass Extinction. *Science* 282(5387):276–279.
26. Hull PM, Norris RD (2011) Diverse patterns of ocean export productivity change across the Cretaceous-Paleogene boundary: New insights from biogenic barium. *Paleoceanography* 26(3):PA3205.
27. Birch HS, Coxall HK, Pearson PN, Kroon D, Schmidt DN (2016) Partial Collapse of the Marine Biological Carbon Pump at the Cretaceous-Palaeogene. *Geology* 44(4):287–290.
28. Culver SJ (2003) Benthic foraminifera across the Cretaceous–Tertiary (K–T) boundary: a review. *Marine Micropaleontology* 47(3):177 – 226.
29. Galbraith ED, Kwon EY, Bianchi D, Hain MP, Sarmiento JL (2015) The impact of atmospheric pCO_2 on carbon isotope ratios of the atmosphere and ocean. *Global Biogeochemical Cycles* 29(3):307–324.
30. Caldeira K, Rampino MR, Volk T, Zachos JC (1990) Biogeochemical modeling at mass extinction boundaries: Atmospheric carbon dioxide and ocean alkalinity at the K/T boundary in *Extinction Events in Earth History*, eds. Kauffman EG, Walliser OH. (Springer-Verlag, Berlin/Heidelberg) Vol. 30, pp. 333–345.
31. Alegret L, Thomas E (2013) Benthic foraminifera across the Cretaceous/Paleogene boundary in the Southern Ocean (ODP Site 690):

Diversity, food and carbonate saturation. *Marine Micropaleontology* 105:40–51.
32. Minoletti F, de Rafelis M, Renard M, Gardin S, Young J (2005) Changes in the pelagic fine fraction carbonate sedimentation during the Cretaceous-Paleocene transition: contribution of the separation technique to the study of Bidart section. *Palaeogeography, Palaeoclimatology, Palaeoecology* 216(1-2):119–137.
33. Steinthorsdottir M, Vajda V, Pole M (2016) Global trends of pCO_2 across the Cretaceous-Paleogene boundary supported by the first Southern Hemisphere stomatal proxy-based pCO_2 reconstruction. *Palaeogeography, Palaeoclimatology, Palaeoecology* 464:143–152.
34. Westerhold T, Röhl U, Donner B, McCarren HK, Zachos JC (2011) A complete high-resolution Paleocene benthic stable isotope record for the central Pacific (ODP Site 1209). *Paleoceanography* 26(2):PA2216.
35. Ridgwell A, et al. (2007) Marine geochemical data assimilation in an efficient Earth System Model of global biogeochemical cycling. *Biogeosciences* 4:87–104.
36. Thomas E (2007) Cenozoic mass extinctions in the deep sea: What perturbs the largest habitat on Earth? in *Special Paper 424: Large Ecosystem Perturbations: Causes and Consequences*. (Geological Society of America) Vol. 424, pp. 1–23.
37. Friedrich O, Meier KJS (2003) Stable isotopic indication for the cyst formation depth of Campanian/Maastrichtian calcareous dinoflagellates. *Micropaleontology* 49(4):375–380.
38. Hull PM (2015) Life in the aftermath of mass extinctions. *Current Biology* 25(19):R941–R952.
39. Arenillas I, Arz JA, Molina E, Dupuis C (2000) An independent test of planktic foraminiferal turnover across the Cretaceous/Paleogene (K/P) boundary at El Kef, Tunisia; catastrophic mass extinction and possible survivorship. *Micropaleontology* 46(1):31–49.
40. D'Hondt S (2005) Consequences of the Cretaceous/Paleogene Mass Extinction for Marine Ecosystems. *Annual Review of Ecology, Evolution, and Systematics* 36(1):295–317.
41. Markwick PJ, Valdes PJ (2004) Palaeo-digital elevation models for use as boundary conditions in coupled ocean–atmosphere GCM experiments: a Maastrichtian (late Cretaceous) example. *Palaeogeography, Palaeoclimatology, Palaeoecology* 213:37–63.
42. Sessa JA, et al. (2015) Ammonite habitat revealed via isotopic composition and comparisons with co-occurring benthic and planktonic organisms. *Proceedings of the National Academy of Sciences* p. 201507554.
43. Frank TD, et al. (2005) The Maastrichtian record from Shatsky Rise (northwest Pacific): A tropical perspective on global ecological and oceanographic changes. *Paleoceanography* 20:PA1008.
44. Kaiho K (1999) Evolution in the test size of deep-sea benthic foraminifera during the past 120 million years. *Marine Micropaleontology* 37:53–65.
45. Larson RL, Steiner MB, Erba E, Lancelot Y (1992) Paleolatitudes and tectonic reconstructions of the oldest portion of the Pacific Plate: a comparative study. *Proceedings of the Ocean Drilling Program, Scientific Results* 129:615–631.
46. Alegret L, Thomas E (2005) Cretaceous/Paleogene boundary bathyal paleo-environments in the central North Pacific (DSDP Site 465), the Northwestern Atlantic (ODP Site 1049), the Gulf of Mexico and the Tethys: The benthic foraminiferal record. *Palaeogeography, Palaeoclimatology, Palaeoecology* 224(1-3):53–82.
47. Alegret L, Thomas E (2009) Food supply to the seafloor in the Pacific Ocean after the Cretaceous/Paleogene boundary event. *Marine Micropaleontology* 73(1-2):105–116.
48. Boersma A, Shackleton NJ (1981) Oxygen and carbon-isotope variations and planktonic-foraminifer depth habitats, Late Cretaceous to Paleocene, Central Pacific, Deep Sea Drilling Project Sites 463 and 465. *Initial Reports of the Deep Sea Drilling Project* 62:513–526.
49. Vallier TL, Rea DK, Dean WE, Thiede J, Adelseck CG (1981) The Geology of Hess Rise, Central North Pacific Ocean. *Initial Reports of the Deep Sea Drilling Project* 62:1031–1061.
50. Alegret L, Thomas E (2004) Benthic foraminifera and environmental turnover across the Cretaceous/Paleogene boundary at Blake Nose (ODP Hole 1049C, Northwestern Atlantic). *Palaeogeography, Palaeoclimatology, Palaeoecology* 208(1-2):59–83.
51. Abramovich S, Keller G, Berner Z, Cymbalista M, Rak C (2011) Maastrichtian planktic foraminiferal biostratigraphy and palaeoenvironment of Brazos River, Falls County, Texas, USA. *SEPM Special Publication* 100:123–156.
52. Hancock HJL, Dickens GR (2005) Carbonate Dissolution Episodes in Paleocene and Eocene Sediment, Shatsky Rise, West-Central Pacific. *Proceedings of the Ocean Drilling Program, Scientific Results* Leg 198.
53. Edgar KM, Anagnostou E, Pearson PN, Foster GL (2015) Assessing the impact of diagenesis on δ^{11}B, δ^{13}C, δ^{18}O, Sr/Ca and B/Ca values in fossil planktic foraminiferal calcite. *Geochimica et Cosmochimica Acta* 166:189–209.
54. Huber BT, Norris RD, MacLeod KG (2002) Deep-sea paleotemperature record of extreme warmth during the Cretaceous. *Geology* 30(2):123–126.
55. Huber BT, MacLeod KG, Tur NA (2008) Chronostratigraphic Framework for Upper Campanian-Maastrichtian Sediments on the Blake Nose (Subtropical North Atlantic). *The Journal of Foraminiferal Research* 38(2):162–182.
56. Vonhof HB, Smit J (1996) Strontium-isotope stratigraphy of the type Maastrichtian and the Cretaceous/Tertiary boundary in the Maastricht area (SE Netherlands). *Geologie en Mijnbouw* 75:275–282.
57. Pearson PN, et al. (2001) Warm tropical sea surface temperatures in the Late Cretaceous and Eocene epochs. *Nature* 413(6855):481–487.
58. Wilson PA, Norris RD, Cooper MJ (2002) Testing the Cretaceous greenhouse hypothesis using glassy foraminiferal calcite from the core of the Turonian tropics on Demerara Rise. *Geology* 30(7):607.
59. Smit J, Zachariasse WJ (1996) Planktic foraminifera in the Cretaceous/Tertiary boundary clays of the Geulhemmerberg (Netherlands). *Geologie en Mijnbouw* 75:187–191.
60. Mai H, v. Salis Perch-Nielsen K, Willems H, Romein T (1997) Fossil Coccospheres from the K/T Boundary Section from Geulhemmerberg, the Netherlands. *Micropaleontology* 43(3):281–302.
61. Hansen TA (1980) Influence of larval dispersal and geographic distribution on species longevity in neogastropods. *Paleobiology* 6(2):193–207.

62. Hansen TA (1988) Early Tertiary radiation of marine molluscs and the long-term effects of the Cretaceous-Tertiary extinction. *Paleobiology* 14(1):37–51.
63. Hart, Malcolm B. and Yancey, Thomas E. and Leighton, Andrew D. and Miller, Brent and Liu, Chengjie and Smart, Christopher W. and Twitchett, Richard J. (2012) The Cretaceous-Paleogene boundary on the Brazos River, Texas: new stratigraphic sections and revised interpretations. *GCAGS Journal* 1:69–80.
64. Yancey TE, Liu C (2013) Impact-Induced Sediment Deposition On An Offshore, Mud-Substrate Continental Shelf, Cretaceous–Paleogene Boundary, Brazos River, Texas, U.S.A. *Journal of Sedimentary Research* 83(4):354–367.
65. Smit J (1999) The Global Stratigraphy of the Cretaceous-Tertiary Impact Ejecta. *Annual Review of Earth and Planetary Sciences* 27:75–113.
66. Kozdon R, et al. (2013) In situ δ^{18}O and Mg/Ca analyses of diagenetic and planktic foraminiferal calcite preserved in a deep–sea record of the Paleocene–Eocene Thermal Maximum. *Paleoceanography* 28(3):517–528.
67. Dinarès-Turell J, Westerhold T, Pujalte V, Röhl U, Kroon D (2014) Astronomical calibration of the Danian stage (Early Paleocene) revisited: Settling chronologies of sedimentary records across the Atlantic and Pacific Oceans. *Earth and Planetary Science Letters* 405:119–131.
68. Gradstein FM, Ogg JG, Schmitz M, Ogg G (2012) *The Geologic Time Scale 2012 2-Volume Set*. (Elsevier).
69. Premoli Silva I, Petrizzo MR, Melloni D (2005) Planktic foraminiferal biostratigraphy across the Cretaceous/Palaeocene Boundary at Shatsky Rise (ODP Leg 198, Northwest Pacific). in *Proceedings of the Ocean Drilling Program, Results*, eds. Bralower TJ, Premoli Silva I, Malone MJ. (ODP), Vol. 198, pp. 1–15 (Online).
70. Brinkhuis H, Schiøler P (1996) Palynology of the Geulhemmerberg Cretaceous/Tertiary boundary section (Limburg, SE Netherlands). *Geologie en Mijnbouw* 75:193–213.
71. Romein AJT, Willems H, Mai H (1996) Calcareous nannoplankton of the Geulhemmerberg K/T boundary section, Maastrichtian type area, The Netherlands. *Geologie en Mijnbouw* 75.
72. Mai H, Speijer RP, Schulte P (2003) Calcareous index nannofossils (coccoliths) of the lowermost Paleocene originated in the late Maastrichtian. *Micropaleontology* 49(2):189–195.
73. Mai H (1999) Paleocene coccoliths and coccospheres in deposits of the Maastrichtian stage at the 'type locality' and type area in SE Limburg, Netherlands. *Marine Micropaleontology* 36(1):1–12.
74. Strong CP (2000) Cretaceous–Tertiary foraminiferal succession at Flaxbourne River, Marlborough, New Zealand. *New Zealand Journal of Geology and Geophysics* 43(1):1–20.
75. Hollis CJ, Strong CP, Rodgers KA, Rogers KM (2003) Paleoenvironmental changes across the Cretaceous/Tertiary boundary at Flaxbourne River and Woodside Creek, eastern Marlborough, New Zealand. *New Zealand Journal of Geology and Geophysics* 46(2):177–197.
76. Landman NH, et al. (2014) Ammonite extinction and nautilid survival at the end of the Cretaceous. *Geology* 42(8):707–710.
77. Smit J, Rocchia R (1996) Neutron Activation analysis of trace elements in the Geulhemmerberg Cretaceous/Tertiary boundary section, SE Netherlands. *Geologie en Mijnbouw* 75(2):269–274.
78. Machalski M, Vellekoop J, Dubicka Z, Peryt D, Harasimiuk M (2016) Late Maastrichtian cephalopods, dinoflagellate cysts and foraminifera from the Cretaceous–Paleogene succession at Lechówka, southeast Poland: Stratigraphic and environmental implications. *Cretaceous Research* 57:208–227.
79. Henriksson AS (1993) Biochronology of the terminal Cretaceous calcareous nannofossil zone of *Micula prinsii*. *Cretaceous Research* 14(1):59–68.
80. Husson D, Galbrun B, Gardin S, Thibault N (2014) Tempo and duration of short-term environmental perturbations across the Cretaceous-Paleogene boundary. *Stratigraphy* 11(2):159–171.
81. Vellekoop J, et al. (2014) Rapid short-term cooling following the Chicxulub impact at the Cretaceous-Paleogene boundary. *Proceedings of the National Academy of Sciences* 111(21):7537–7541.
82. Schulte P, Speijer RP, Mai H, Kontny A (2006) The Cretaceous–Paleogene (K–P) boundary at Brazos, Texas: Sequence stratigraphy, depositional events and the Chicxulub impact. *Sedimentary Geology* 184(1-2):77–109.
83. Rae JW, Foster GL, Schmidt DN, Elliott T (2011) Boron isotopes and B/Ca in benthic foraminifera: Proxies for the deep ocean carbonate system. *Earth and Planetary Science Letters* 302(3-4):403–413.
84. Wendler I, Huber BT, MacLeod KG, Wendler JE (2013) Stable oxygen and carbon isotope systematics of exquisitely preserved Turonian foraminifera from Tanzania - Understanding isotopic signatures in fossils. *Marine Micropaleontology* 102:1–33.
85. Foster GL (2008) Seawater pH, pCO_2 and $[CO_3^{2-}]$ variations in the Caribbean Sea over the last 130kyr: A boron isotope and B/Ca study of planktic foraminifera. *Earth and Planetary Science Letters* 271(1-4):254–266.
86. Zhang S, et al. (2016) Investigating controls on boron isotope ratios in shallow marine carbonates. *Earth and Planetary Science Letters* 458:380–393.
87. Henehan MJ, et al. (2013) Calibration of the boron isotope proxy in the planktonic foraminifera *Globigerinoides ruber* for use in palaeo-CO_2 reconstruction. *Earth and Planetary Science Letters* 364:111–122.
88. Okai T, Suzuki A, Kawahata H, Terashima S, Imai N (2002) Preparation of a New Geological Survey of Japan Geochemical Reference Material: Coral JCp-1. *Geostandards Newsletter* 26(1):95–99.
89. Inoue M, Nohara M, Okai T, Suzuki A, Kawahata H (2004) Concentrations of Trace Elements in Carbonate Reference Materials Coral JCp-1 and Giant Clam JCt-1 by Inductively Coupled Plasma-Mass Spectrometry. *Geostandards and Geoanalytical Research* 28(3):411–416.
90. Vogl J, Rosner M (2012) Production and Certification of a Unique Set of Isotope and Delta Reference Materials for Boron Isotope

Determination in Geochemical, Environmental and Industrial Materials. *Geostandards and Geoanalytical Research* 36(2):161–175.
91. Hull PM, Norris RD, Bralower TJ, Schueth JD (2011) A role for chance in marine recovery from the end-Cretaceous extinction. *Nature Geoscience* 4(12):856–860.
92. Schouten S, Huguet C, Hopmans EC, Kienhuis MV, Sinninghe Damsté JS (2007) Analytical methodology for TEX_{86} paleothermometry by high–performance liquid chromatography/atmospheric pressure chemical ionization mass spectrometry. *Analytical Chemistry* 79:2940–2944.
93. Hopmans EC, Schouten S, Damsté JSS (2016) The effect of improved chromatography on GDGT-based palaeoproxies. *Organic Geochemistry* 93:1–6.
94. Schouten S, Hopmans EC, Schefuß E, Damsté JSS (2002) Distributional variations in marine crenarchaeotal membrane lipids: a new tool for reconstructing ancient sea water temperatures? *Earth and Planetary Science Letters* 204(1-2):265–274.
95. Kim JH, et al. (2010) New indices and calibrations derived from the distribution of crenarchaeal isoprenoid tetraether lipids: Implications for past sea surface temperature reconstructions. *Geochimica et Cosmochimica Acta* 74(16):4639–4654.
96. De Jonge C, et al. (2014) Occurrence and abundance of 6-methyl branched glycerol dialkyl glycerol tetraethers in soils: Implications for palaeoclimate reconstruction. *Geochimica et Cosmochimica Acta* 141(97-112).
97. Naafs BDA, et al. (2017) Introducing global peat-specific temperature and pH calibrations based on brGDGT bacterial lipids. *Geochimica et Cosmochimica Acta* 208:285–301.
98. Sanyal A, Bijma J, Spero HJ, Lea DW (2001) Empirical relationship between pH and the boron isotopic composition of *Globigerinoides sacculifer*: Implications for the boron isotope paleo-pH proxy. *Paleoceanography* 16:515–519.
99. Henehan MJ, et al. (2016) A new boron isotope-pH calibration for *Orbulina universa*, with implications for understanding and accounting for 'vital effects'. *Earth and Planetary Science Letters* 454:282–292.
100. D'Hondt S, Arthur MA (1995) Interspecies variation in stable isotopic signals of Maastrichtian planktonic foraminifera. *Paleoceanography* 10(1):123–135.
101. Bornemann A, Norris RD (2007) Size-related stable isotope changes in Late Cretaceous planktic foraminifera: Implications for paleoecology and photosymbiosis. *Marine Micropaleontology* 65:32–42.
102. Leckie RM (1987) Paleoecology of Mid-Cretaceous Planktonic Foraminifera: A Comparison of Open Ocean and Epicontinental Sea Assemblages. *Micropaleontology* 33(2):164–176.
103. D'Hondt S, Zachos JC (1998) Cretaceous foraminifera and the evolutionary history of planktic photosymbiosis. *Paleobiology* 24(4):512–523.
104. Martínez-Botí MA, et al. (2015) Boron isotope evidence for oceanic carbon dioxide leakage during the last deglaciation. *Nature* 518(7538):219–222.
105. Falzoni F, Petrizzo MR, Clarke LJ, MacLeod KG, Jenkyns HC (2016) Long-term Late Cretaceous oxygen- and carbon-isotope trends and planktonic foraminiferal turnover: A new record from the southern midlatitudes. *GSA Bulletin*.
106. Abramovich S, Yovel-Corem S, Almogi-Labin A, Benjamini C (2010) Global climate change and planktic foraminiferal response in the Maastrichtian. *Paleoceanography* 25:PA2201.
107. Timofeeff MN, Lowenstein TK, Martins da Silva MA, Harris NB (2006) Secular variation in the major–ion chemistry of seawater: Evidence from fluid inclusions in Cretaceous halites. *Geochimica et Cosmochimica Acta* 70(8):1977–1994.
108. Brennan ST, Lowenstein TK, Cendón DI (2013) The major-ion composition of Cenozoic seawater: The past 36 million years from fluid inclusions in marine halite. *American Journal of Science* 313(8):713–775.
109. Gothmann AM, et al. (2015) Fossil corals as an archive of secular variations in seawater chemistry since the Mesozoic. *Geochimica et Cosmochimica Acta* 160:188–208.
110. Evans D, Brierley C, Raymo ME, Erez J, Müller W (2016) Planktic foraminifera shell chemistry response to seawater chemistry: Pliocene-Pleistocene seawater Mg/Ca, temperature and sea level change. *Earth and Planetary Science Letters* 438:139–148.
111. Zachos JC, Stott LD, Lohmann KC (1994) Evolution of early Cenozoic marine temperatures. *Paleoceanography* 9(2):353–387.
112. Cramer BS, Miller KG, Barrett PJ, Wright JD (2011) Late Cretaceous–Neogene trends in deep ocean temperature and continental ice volume: Reconciling records of benthic foraminiferal geochemistry (δ^{18}O and Mg/Ca) with sea level history. *Journal of Geophysical Research* 116:C12023.
113. Lear CH, Rosenthal Y, Slowey N (2002) Benthic foraminiferal Mg/Ca-paleothermometry: a revised core-top calibration. *Geochimica et Cosmochimica Acta* 66(19):3375–3387.
114. Evans D, Wade BS, Henehan M, Erez J, Müller W (2016) Revisiting carbonate chemistry controls on planktic foraminifera Mg/Ca: implications for sea surface temperature and hydrology shifts over the Paleocene–Eocene Thermal Maximum and Eocene–Oligocene transition. *Clim. Past* 12(4):819–835.
115. R Core Team (2017) *R: A language and environment for statistical computing, v.3.4.2* (R Foundation for Statistical Computing, Vienna, Austria).
116. Hain MP, Sigman DM, Higgins JA, Haug GH (2015) The effects of secular calcium and magnesium concentration changes on the thermodynamics of seawater acid/base chemistry: Implications for Eocene and Cretaceous ocean carbon chemistry and buffering. *Global Biogeochemical Cycles* p. 2014GB004986.
117. Lemarchand D, Gaillardet J, Lewin É, Allègre CJ (2002) Boron isotope systematics in large rivers: implications for the marine boron budget and paleo-pH reconstruction over the Cenozoic. *Chemical Geology* 190(1-4):123–140.
118. Millero FJ (1995) Thermodynamics of the carbon dioxide system in the oceans. *Geochimica et Cosmochimica Acta* 59(4):661–677.
119. Orr JC, Epitalon JM, Gattuso JP (2015) Comparison of ten packages that compute ocean carbonate chemistry. *Biogeosciences* 12:1483–1510.

120. Zeebe RE, Wolf-Gladrow D (2001) *CO_2 in seawater: Equilibrium, Kinetics, Isotopes*, Elsevier Oceanography Series. (Elsevier, Amsterdam) No. 65.
121. Hönisch B, Hemming NG, Archer D, Siddall M, McManus JF (2009) Atmospheric Carbon Dioxide Concentration Across the Mid-Pleistocene Transition. *Science* 324(5934):1551–1554.
122. Zeebe RE (2012) LOSCAR: Long-term Ocean-atmosphere-Sediment CArbon cycle Reservoir Model v2.0.4. *Geosci. Model Dev.* 5(1):149–166.
123. Simon L, Lécuyer C, Maréchal C, Coltice N (2006) Modelling the geochemical cycle of boron: Implications for the long-term δ^{11}B evolution of seawater and oceanic crust. *Chemical Geology* 225:61–76.
124. Greenop R, et al. (2017) A record of Neogene seawater δ^{11}B reconstructed from paired δ^{11}B analyses on benthic and planktic foraminifera. *Climate of the Past* 13(2):149–170.
125. Foster GL, Strandmann PAEPv, Rae JWB (2010) Boron and magnesium isotopic composition of seawater. *Geochemistry Geophysics Geosystems* 11:10 PP.
126. Anagnostou E, et al. (2016) Changing atmospheric CO_2 concentration was the primary driver of early Cenozoic climate. *Nature* 533:380–384.
127. Pearson PN, Palmer MR (2000) Atmospheric carbon dioxide concentrations over the past 60 million years. *Nature* 406(6797):695–699.
128. Battino R, Rettlich TR, Tominaga T (1983) The solubility of oxygen and ozone in liquids. *Journal of Physical and Chemical Reference Data* 12:163–178.
129. Hull PM, Osborn KJ, Norris RD, Robinson BH (2011) Seasonality and depth distribution of a mesopelagic foraminifer, *Hastigerina digitata*, in Monterrey Bay, California. *Limnology and Oceanography* 56:562–576.
130. Zeebe RE, Westbroek P (2003) A simple model for the $CaCO_3$ saturation state of the ocean: The "Strangelove," the "Neritan," and the "Cretan" Ocean. *Geochemistry, Geophysics, Geosystems* 4(12):n/a–n/a.
131. Ridgwell AJ, Zeebe RE (2005) The role of the global carbonate cycle in the regulation and evolution of the Earth system. *Earth and Planetary Science Letters* 234(3-4):299–315.
132. D'Hondt S, Inagaki F, Alvarez-Zarikian CA, Expedition 329 Scientists (2011) South Pacific Gyre Subseafloor Life. *Proceedings of the Integrated Ocean Drilling Program* 329.
133. Berger WH, et al. (1992) The record of Ontong Java Plateau: Main results of ODP Leg 130. *Geological Society of America Bulletin* 104(8):954–972.
134. Schoene B, et al. (2015) U-Pb geochronology of the Deccan Traps and relation to the end-Cretaceous mass extinction. *Science* 347(6218):182–184.
135. Renne PR, et al. (2015) State shift in Deccan volcanism at the Cretaceous-Paleogene boundary, possibly induced by impact. *Science* 350(6256):76–78.
136. Chenet AL, Quidelleur X, Fluteau F, Courtillot V, Bajpai S (2007) ^{40}K–^{40}Ar dating of the Main Deccan large igneous province: Further evidence of KTB age and short duration. *Earth and Planetary Science Letters* 263(1-2):1–15.
137. Dessert C, et al. (2001) Erosion of Deccan Traps determined by river geochemistry: impact on the global climate and the ^{87}Sr/^{86}Sr ratio of seawater. *Earth and Planetary Science Letters* 188(3-4):459–474.
138. Gutjahr M, et al. (2017) Very large release of mostly volcanic carbon during the Palaeocene–Eocene Thermal Maximum. *Nature* 548(7669):573–577.
139. Misra S, Froelich PN (2012) Lithium Isotope History of Cenozoic Seawater: Changes in Silicate Weathering and Reverse Weathering. *Science* 335(6070):818–823.
140. Vigier N, et al. (2014) New Constraints on K-Pg boundary Environmental Changes with Lithium Isotopes in *AGU Fall Meeting Abstracts*. (AGU, San Francisco), Vol. 1, pp. PP51B–1124.
141. Roberts J, et al. (2018) Lithium isotopic composition of benthic foraminifera: A new proxy for paleo-pH reconstruction. *Geochimica et Cosmochimica Acta* 236:336–350.
142. Dickson AG, Goyet C, eds. (1994) *Handbook of methods for the analysis of the various parameters of the carbon dioxide system in sea water*. (Oak Ridge National Laboratories/Carbon Dioxide Information and Analysis Center in Oak Ridge, Tennessee, USA) Vol. version 2.1.
143. Cao L, et al. (2009) The role of ocean transport in the uptake of anthropogenic CO_2. *Biogeosciences* 6(3):375–390.
144. Monteiro FM, Pancost RD, Ridgwell A, Donnadieu Y (2012) Nutrients as the dominant control on the spread of anoxia and euxinia across the Cenomanian-Turonian oceanic anoxic event (OAE2): Model-data comparison. *Paleoceanography* 27(4).
145. Niezgodzki I, Tyszka J, Knorr G, Lohmann G (2019) Was the Arctic Ocean ice free during the latest Cretaceous? The role of CO_2 and gateway configurations. *Global and Planetary Change* 177:201–212.
146. Baatsen MLJ, von der Heydt AS, Kliphuis M, Viebahn J, Dijkstra HA (2018) Multiple states in the late Eocene ocean circulation. *Global and Planetary Change* 163:18–28.
147. Hutchinson DK, et al. (2018) Climate sensitivity and meridional overturning circulation in the late Eocene using GFDL CM2.1. *Climate of the Past* 14(6):789–910.
148. Niezgodzki I, Knorr G, Lohmann G, Tyszka J, Markwick PJ (2017) Late Cretaceous climate simulations with different CO_2 levels and subarctic gateway configurations: A model data comparison. *Paleoceanography* 32(9):980–998.
149. Norris R, Wilson D, Blum P, the Expedition 342 Scientists, eds. (2014) *Proceedings of the Integrated Ocean Drilling Program, 342 Initial Reports*, Proceedings of the Ocean Drilling Program. (Ocean Drilling Program, College Station, TX) Vol. 342.
150. Schmitz B, Keller G, Stenvall O (1992) Stable isotope and foraminiferal changes across the Cretaceous–Tertiary boundary at Stevns Klint, Denmark: Arguments for long-term oceanic instability before and after bolide–impact event. *Palaeogeography, Palaeoclimatology,*

Palaeoecology 96(3-4):233–260.
151. Hart MB, et al. (2005) The Cretaceous–Palaeogene boundary succession at Stevns Klint, Denmark: Foraminifers and stable isotope stratigraphy. *Palaeogeography, Palaeoclimatology, Palaeoecology* 224(1-3):6–26.
152. Hunter SJ, Valdes PJ, Haywood AM, Markwick PJ (2008) Modelling Maastrichtian climate: investigating the role of geography, atmospheric CO_2 and vegetation. *Climate of the Past Discussions* 4:981–1019.
153. Tyrrell T, Zeebe RE (2004) History of carbonate ion concentration over the last 100 million years. *Geochimica et Cosmochimica Acta* 68(17):3521–3530.
154. Lowenstein TK, Hardie LA, Timofeeff MN, Demicco RV (2003) Secular variation in seawater chemistry and the origin of calcium chloride basinal brines. *Geology* 31(10):857.
155. Panchuk K, Ridgwell A, Kump L (2008) Sedimentary response to Paleocene-Eocene Thermal Maximum carbon release: A model-data comparison. *Geology* 36(4):315 –318.
156. Taylor LL, Banwart SA, Valdes PJ, Leake JR, Beerling DJ (2012) Evaluating the effects of terrestrial ecosystems, climate and carbon dioxide on weathering over geological time: a global-scale process-based approach. *Philosophical Transactions of the Royal Society B: Biological Sciences* 367(1588):565–582.
157. Thomas DJ (2004) Evidence for deep-water production in the North Pacific Ocean during the early Cenozoic warm interval. *Nature* 430(6995):65–68.
158. Marchal O, Stocker TF, Fortunate J (2002) A latitude–depth, circulation–biogeochemical ocean model for paleoclimate studies. development and sensitivities. *Tellus B* 50(3):290–316.
159. Kwon EY, Primeau F, Sarmiento JL (2009) The impact of remineralization depth on the air–sea carbon balance. *Nature Geoscience* 2(9):630–635.
160. Meyer KM, Ridgwell A, Payne JL (2016) The influence of the biological pump on ocean chemistry: implications for long-term trends in marine redox chemistry, the global carbon cycle, and marine animal ecosystems. *Geobiology* 14(3):207–219.
161. Jiang S, Bralower TJ, Patzkowsky ME, Kump LR, Schueth JD (2010) Geographic controls on nannoplankton extinction across the Cretaceous/Palaeogene boundary. *Nature Geoscience* 3(4):280–285.